BRNO UNIVERSITY OF TECHNOLOGY
VYSOKÉ UČENÍ TECHNICKÉ V BRNĚ

FACULTY OF ELECTRICAL ENGINEERING AND COMMUNICATION
FAKULTA ELEKTROTECHNIKY
A KOMUNIKAČNÍCH TECHNOLOGIÍ

DEPARTMENT OF BIOMEDICAL ENGINEERING
ÚSTAV BIOMEDICÍNSKÉHO INŽENÝRSTVÍ

DEFINITION OF PARAMETERS FOR IMAGE DECONVOLUTION FROM ELECTRON MICROSCOPE
DEFINICE PARAMETRU PRO DEKONVOLUCI OBRAZU Z ELEKTRONOVÉHO MIKROSKOPU

MASTER'S THESIS
DIPLOMOVÁ PRÁCE

AUTHOR — **Bc. Viktor Typovský**
AUTOR PRÁCE

SUPERVISOR — **Ing. Tomáš Potočňák**
VEDOUCÍ PRÁCE

BRNO 2018

BRNO UNIVERSITY OF TECHNOLOGY
FACULTY OF ELECTRICAL ENGINEERING AND COMMUNICATION

Master's Thesis

Master's study field **Biomedical and Ecological Engineering**
Department of Biomedical Engineering

Student: Bc. Viktor Typovský ***ID:*** 162832

Year of study: 2 ***Academic year:*** 2017/18

TITLE OF THESIS:

Definition of Parameters for Image Deconvolution from Electron Microscope

INSTRUCTION:

1) Elaborate a literary research for blind image deconvolution. Study the electron microscope imaging modes and discuss the impact of its individual parts on the distortion of the resulting image. 2) Design a model of deconvolution kernel for an electron microscope scanning mode. Choose the optimal image deconvolution method. 3) Design an evaluation procedure of the results and their dependence on acquisition parameters of the electron microscope. 4) Take pictures in collaboration with FEI Czech Republic. 5) Test the suggested methods on model and real images and compare them with the method available in commercially used software. 6) Discuss the results obtained and evaluate the effectiveness and usability of the methods. The diploma thesis is created in cooperation with FEI Czech Republic (part of Thermo Fisher Scientific).

RECOMMENDED LITERATURE:

[1] KARLIK M., Úvod do transmisní elektronové mirkoskopie. Praha ČVUT, 2011. ISBN 978-80-01-04729-3.

[2] CAMPISI, P., Egiazarian, K., Blind Image Deconvolution“ Theory and Applications. CRC Press: Boca Raton: 2007, 114 s. ISBN 978-1-4200-0729-9.

Date of project specification: 5.2.2018 ***Deadline for submission:*** 18.5.2018

Leader: Ing. Tomáš Potočňák
Consultant: Ing. Miloš Malínský, Ph.D.

prof. Ing. Ivo Provazník, Ph.D.
Subject Council chairman

ABSTRAKT

Tato diplomová práce se zabývá modelováním bodové rozptylové funkce (point spread function, PSF) u skenovacího transmisního elektronového mikroskopu (STEM). Nejprve je provedena teoretická rešerše, kde jsou popsány všechny důležitě aspekty, potřebné k následnému modelování. Je tedy proveden základní popis konstrukce přístroje a určeny jeho klíčové komponenty, které mají hlavní vliv na tvar výsledné PSF. Následně jsou popsány hlavní zobrazovací vady, které ovlivňují výslednou PSF. Ty jsou popsány z hlediska vlnové optiky. Na základě toho je pak navržen a zrealizován poměrně přesný model PSF u mikroskopu STEM. Poté je vytvořeno GUI, které umožňuje plné využití daného vytvořeného modelu. Na závěr je získaný model otestován na modelových a reálných datech, pomocí metody Lucy-Richardson.

KLÍČOVÁ SLOVA

skenovácí transmisní elektronový mikroskop (STEM), dekonvoluce obrazu, zobrazovací vady, point spread function(PSF), vlnová optika, model, simulace

ABSTRACT

This master thesis deals with the point spread function (PSF) modelling of a Scanning Transmission Electron Microscope (STEM). First, the theoretical research is performed, describing all the important aspects, that are necessary for following modelling. Thus, the basic description of the construction of this device is performed. Than its key components are determined, which have a major influence on the shape of the resultant PSF. Subsequently, the main imaging aberrations that affect the resulting PSF are described. These are described in terms of wave optics. In this base, the relatively accurate PSF model of the STEM microscope is designed and realized. Then, the GUI is created which allows full use of the created model. Finally, the obtained model is tested on model and real data using the Lucy-Richardson method.

KEYWORDS

scanning transmission electron microscope (STEM), image deconvolution, imaging aberrations, point spread function (PSF), wave optics, model, simulation

TYPOVSKÝ, V. *Definice parametru pro dekonvoluci obrazu z elektronového mikroskopu*. Brno: Vysoké učení technické v Brně, Fakulta elektrotechniky a komunikačních technologií, Ústav biomedicínského inženýrství, 2018. 11 s., 3 s. příloh. Diplomové práce. Vedoucí práce: Ing. Tomáš Potočňák.

PROHLÁŠENÍ

Prohlašuji, že svoji diplomovou práci na téma Definice parametru pro dekonvoluci obrazu z elektronového mikroskopu jsem vypracoval samostatně pod vedením vedoucího semestrální práce a s použitím odborné literatury a dalších informačních zdrojů, které jsou všechny citovány v práci a uvedeny v seznamu literatury na konci práce.

Jako autor uvedené diplomové práce dále prohlašuji, že v souvislosti s vytvořením této diplomové práce jsem neporušil autorská práva třetích osob, zejména jsem nezasáhl nedovoleným způsobem do cizích autorských práv osobnostních a/nebo majetkových a jsem si plně vědom následků porušení ustanovení § 11 a následujících zákona č. 121/2000 Sb., o právu autorském, o právech souvisejících s právem autorským a o změně některých zákonů (autorský zákon), ve znění pozdějších předpisů, včetně možných trestněprávních důsledků vyplývajících z ustanovení části druhé, hlavy VI. díl 4 Trestního zákoníku č. 40/2009 Sb.

V Brně dne ....

(podpis autora)

PODĚKOVÁNÍ

Tímto bych chtěl poděkovat vedoucímu mé diplomové práce panu
Ing. Tomáši Potočňákovi za účinnou odbornou pomoc při zpracování této práce. Dále bych však chtěl především poděkovat panu Ing. Miloši Malínskému, Ph.D. a panu Mgr. Janovi Jíšovi za cennou a velice účinnou pomoct při zpracování této diplomové práce.

CONTENTS

LIST OF FIGURES

Final aberration that is incorporated to the calculation is influence of partial temporal coherence and thus influence of chromatic aberration of the objective lens and energy spread of the electron source, described by the Gaussian

LIST OF TABLES

INTRODUCTION

Nowadays we meet with various achievements. These can be i.e. some modern supermaterials, amazing hi-tech devices or a miracle cure. However, behind these is science. And where would the science be without a microscope? This device allows us to look into the microcosm beyond the limits of our own eyes. This is the key to a deeper understanding of various things. So, when these great devices improve, they allow us to look deeper. However, these devices also have their limits, especially in terms of physics. Nevertheless, these limitations can be circumvented or corrected by a software solution. One of this solution is the deconvolution. Its aim is to correct distortion in the image acquired by the imaging device, which is limited by certain unavoidable aberrations. Captured image is thus always distorted relative to the scene.

This thesis deals especially with the application of the non-blind deconvolution. It tries to modify the image in order to this image resembles as much as possible to the scanned scene. In other words, it tries to eliminate the distortion caused by imaging aberrations of given imaging device. This approach, however, requires prior knowledge of the nature of the distortion of the imaging system. This is the reason why a deeper theoretical analysis is needed.

The first section describes the general basis of transmission electron microscopy and the STEM instrument including components that have major effect to image creation and distortion.

In the second section, aberrations of these components are described theoretically in detail. They are described from a geometrical point of view to better understanding. However, they are also described from a wave optical point of view, which is crucial in this this case. Finally, the summary of the effect of these aberrations is performed.

The third section discusses the acquisition parameters that most affect the acquired image.

In the fourth section, there are described the distortion model, the point spread function (PSF) and some non-blind deconvolution methods.

The fifth section describes the method of evaluating of deconvolution results.

The section six describes individual steps of PSF realization. It starts with the diffraction model realization and then other imaging aberrations are added.

In the section seven, is presented verifying of functioning of evaluation methods. Then the noise estimation is described and finally, the results are presented.

1 TRANSMISSION ELECTRON MICROSCOPY

1.1 General basics

A microscope is an instrument that consists of several lenses and apertures in order to magnify an image. Its resolution is defined as the smallest distance at which two objects are still recognisable. Maximal theoretical resolution is equal to half of wavelength of the radiation that is used [26].

In 1930s, the French physics de Broglie discovered that electrons can travel in a wave-like fashion identical to that of light. It was great discovery, which means that the light in optical microscopes could be replaced by electrons, so that it opens the gate for the development of electron microscopes. Wavelength of electrons is significantly smaller than wavelength of the light, which means that the maximal achievable resolution of electron microscopes is significantly higher. This is the main reason for using electron microscopes instead of light microscopes.

Transmission electron microscope (TEM) captures the image of thin specimen, which is radiated through by accelerated electrons. If the microscope is equipped with a RTG spectrometer of spectrometer of electron energy losses, the chemical analysis can also be performed. The TEM consists of the electron source, which is at the top position of the system. Then there are the lensing system and system of apertures that focus the beam on the specimen which is then projected onto the viewing screen. In whole microscope, there must be a vacuum. The reasons are: dispersion of electrons in atmosphere, insulation, contamination and work conditions for electron source. The major use of TEM is to examine certain specimens in sub-nanometers detail. The most of these specimens are biological materials, however specimens from chemistry, material science, geology or electronics can be examined too [1][26].

1.2 STEM construction

The scanning transmission electron microscope (STEM) focuses electrons to the very small spot (probe) onto a thin specimen. This means that the image is not captured directly as it is in the case of TEM, but the electron probe moves in the raster and the image is captured gradually. In the case of STEM, its part that is above the specimen is more important, because it forms the electron probe, which is crucial for whole STEM imaging. In the case of TEM it is vice versa, because the projection of electrons that passed the sample is important there.

Modern TEM is usually equipped with the STEM mode, which can be switched. Although, the STEM can be also separate device. This device consists of system of lenses and apertures, as well as the TEM. The purpose of the system of lenses is to provide sufficient demagnification of the electron source in order to obtain an enough small electron probe. [3]

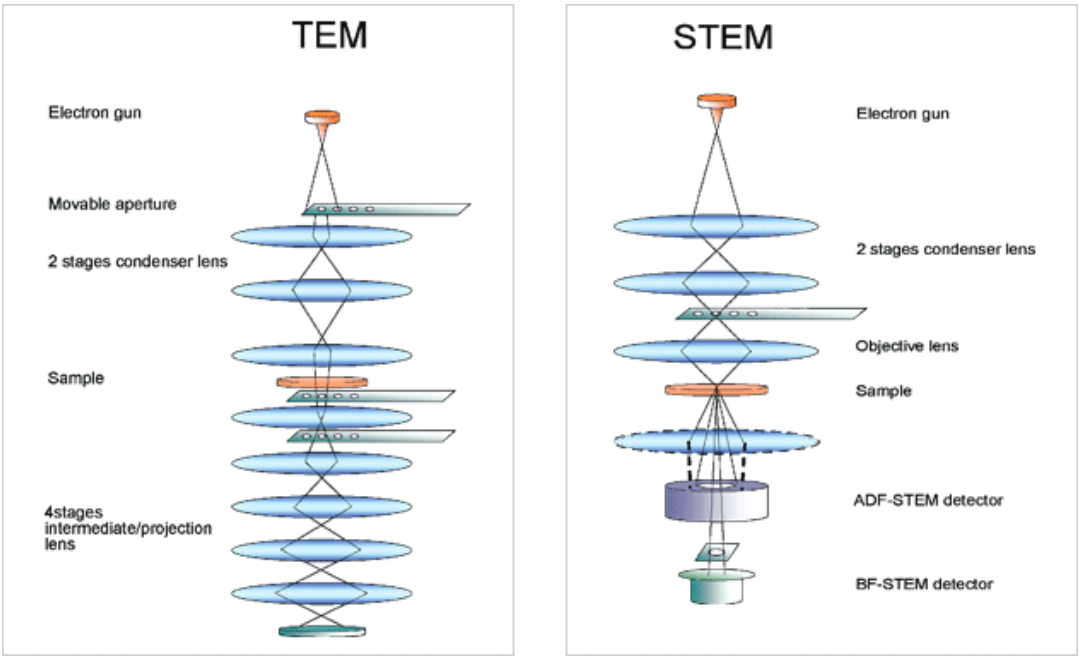

Figure 1.1: TEM and STEM scheme [27]

The optical system contains electron source, condenser lens, objective aperture, objective lens, diffraction lens, deflectors and stigmators.

The electron source emits electrons and its choose is very important. More information about electron sources is described in the section below.

The magnetic lenses are constructed as standard electron lenses. Compared to the objective lens, the condenser and diffraction lens are relatively weak, so that their affect to the final beam formation could be insignificant. On the other hand, the whole effect of the objective cannot be negligible. The condenser lens is used to obtain a parallel beam that is then properly modified by the objective lens. The objective lens is the final focusing lens, that ensures the final and largest demagnification and thus its aberrations are dominant. The diffraction lens is located below the objective lens and specimen. It ensures correct targeting of electrons on detectors when lens focus of the objective lens changes [2][3].

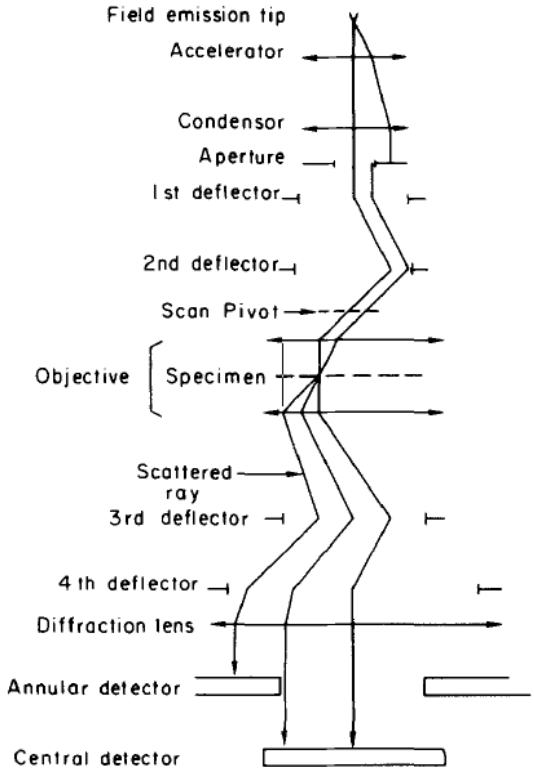

Figure 1.2: STEM scheme [3]

The condensor aperture is in the gap of the condenser lens. The reason why this aperture is placed here (above the deflection coils) and not in the gap on of the objective lens is that, this gap would be too small for objective lens, this aperture and for specimen, which has to be placed here. Moreover, this placing allows to correct some of the lens aberrations. However, the objective aperture is used mainly to control and restrict the amount of beam current and for control of the convergence angle. Even though, its present is necessary, it causes a diffraction aberration which significantly influences the final electron probe [3].

Since this is scanning device, it needs to have deflectors in order to move with the electron beam. It has double deflection scanning system above the objective lens. However, in order to return the beam to the optic axis, there needs to be another set of deflectors, which is located below the objective lens. The deflectors are small magnetic coils, which are driven by current. They are situated in the gap of the objective lens together with stigmator. Each deflector consists of an opposing pair of coils for the *x* coordinate and another pair for the *y*. Raster scanning has the advantage that the signal obtained in each position is easily assigned to a pixel. However, due to deformations that may occur, the actual position of the probe does not correspond to the desired position. This is caused, for example, by drift or non-linearity due to the non-homogeneous magnetic field of these small coils. The accuracy is inversely proportional to the scanning speed [3].

All electron lenses suffer from astigmatism. This aberration is treated by the stigmators. In the case of STEM, the condenser stigmator is used because it is placed in front of the specimen. Other stigmators are located below the specimen and they are thus useless. Stigmator is the quadrupole lens, that is placed around the electron beam. It consists of four magnetic poles: two north poles and two south poles opposite one another. They focus the electron beam in one direction and in another (perpendicular) direction they defocus it, to correct the astigmatism. There are usually used more than one quarupole to treat the astigmatism in more orientations [3][4]

The image that is captured using STEM is called the micrograph. It is 2D array of data points, which each corresponds to the detector signal from certain dwell time. The information that is captured depends on the position of the detector in the diffraction plane [5][6].

There are three types of detectors in the diffraction plane that are circularly separated. Each of them covers certain area of the diffraction plane. It is necessary because if we have one large detector that detects all electrons and the information value about specimen would be zero. Then we can choose which part of the intensity of the diffraction plane we would to capture. The choice of this area then determines the image contrast [5][6].

For the forward scattered electrons, there is the circular detector that provides the bright field (BF) STEM micrograph. This detector gives the maximum signal, when there is no scatterer in the path of the beam.

On the other hand, the ADF (annular dark-field) detector gives the signal that rises, when there is a scatterer in the path of the beam that deflects this beam by certain angle, which is still covered by this detector. This signal also rises with increase of thickness of the specimen. The BF signal and ADF signal are complementary to each other. This means that, if there is for example a scaterrer in the path of the beam, the ADF signal rises but the BF signal decreases and vice versa.

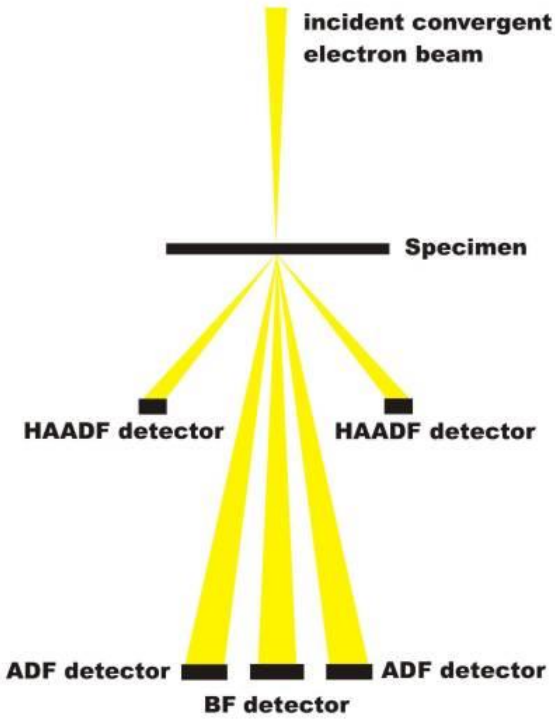

Figure 1.3: STEM detectors [6]

However, if there is a very strong scatterer in the path of the beam, this beam is deflected by higher angle than it is still covered by ADF detector. The HAADF (high angle annular dark-field) detector captures this beam which is deflected by the strong Coulomb interaction. This detector collects electrons which are not Bragg scattered, but they are rather Rutherford scattered, so that the signal that is provided by them is approximately proportional to Z^2 (Z = atomic number) [5][6].

Finally, we can summarize that the electron source, the objective lens aberrations and the illuminating aperture have the most significant effect to the whole STEM imaging.

1.3 Electron gun

The main characteristic of an electron gun is the brightness B (A · m $^{-2}$ · sr^{-1}). It is the current of electrons I (A) related to the electron source size S (m^2) and to the spatial angle Ω (sr), in which the electrons are emitted.

$$B = \frac{I}{S\Omega} = \frac{4I}{\pi^2 \alpha_0^2 d_z^2} \tag{1.1}$$

α_0 (rad) is the illumination angle of the electron beam and d_z (m) is the diameter of an electron source [1].

The brightness significantly distinguish from the intensity of light. The intensity of light can be rather considered as total emission current. The brightness is considered as the beam intensity related to the size of emission surface. For small sizes of electron sources, the brightness rises. It can be also considered as a current of electron beam related to very small window with diameter e.g. 1 nm. So when the brightness is high, there is more current in this very small window. It could also look like some kind of current density [1].

There are two main kinds of electron guns: the thermionic electron guns and the field emission electron guns. Thermionic electron guns consist of a cathode, negative polarized Wehnelt cylinder and grounded anode. Electrons are emitted by heating of the cathode and then they go through the hole of the Wehnelt cylinder, which is used as an electrostatic lens. Thus, the electrons converge in a crossover between the cathode and the anode. The size of the crossover defines the electron source size.

The most common thermionic cathode is thin V-shaped wolfram filament. Another thermionic cathode is lanthanum hexaboride LaB_6 which allows higher the brightness B, but it is more expensive and requires higher vacuum [1].

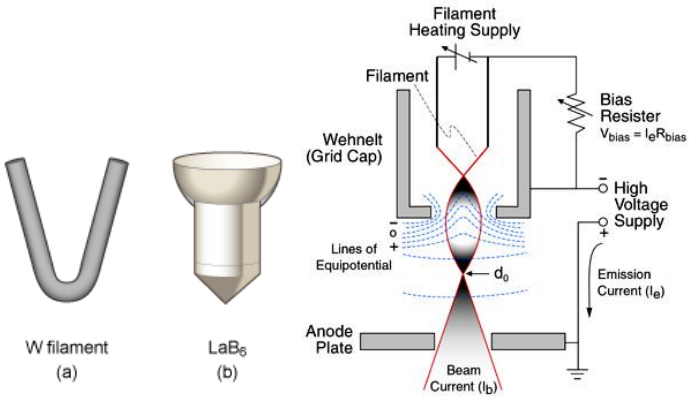

Figure 1.4: Wolfam filament and LaB_6 electron source with thermionic electron source scheme [28][29]

On the other hand, field emission guns have pointed cathode made of wolfram monocrystal. The emission of electrons occurs by tunnel phenomenon due to effect of strong electric field. The source size that is produced by these sources is very small. Moreover, the illumination angle is much smaller, so that, the brightness is very high. However, the total emission current is lower.

The cold field emission gun (CFEG) requires high ultravacuum to slow down its degradation. Another type of FEG, the Schotky thermal field emission sources are significantly more stable and they does not require so high ultra-vacuum. They work at higher temperature, which stabilize and support the emission that is based on the Schotky effect. However, their brightness is quite smaller [1].

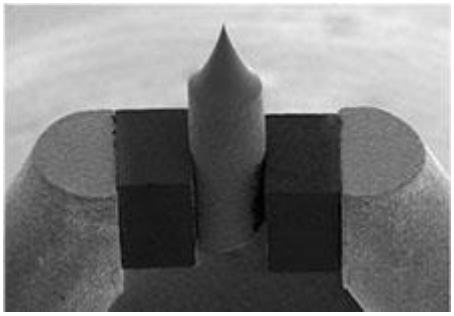

Figure 1.5 Field emission gun **Chyba! Nenalezen zdroj odkazů.**

Table 1: The parameters of different types of electron guns.

Electron gun	Thermionic		Field emission	
Cathode	W filament	LaB6	Schottky	CFEG
Brightness [$A \cdot m^{-2} \cdot sr^{-1}$]	10^9	10^{10}	5×10^{12}	10^{11} - 10^{13}
Current in beam of diameter 1 nm [pA]	0.1	1	500	100 - 1000
Total beam current [nA]	1000	1000	300	10
Electron source size [µm]	50	10	0.03	0.005
Energy dispersion of electrons ΔE [eV]	3	1.5	0.3 - 1	0.3
Working temperature [K]	2700	1900	1800	300
Vacuum [Pa]	10^{-3}	10^{-5}	10^{-6} - 10^{-7}	10^{-8}
Cathode lifetime [h]	40 - 100	500 – 1000	>2000	>2000
Calibration of cathode	no	no	no	after 8 hours

In the case of STEM, one of the most important parameters of electron source is the brightness, because the STEM projects and demagnifies the electron source on the specimen as the demagnified image of the source. However, this demagnification is at the expense of the probe current, which depends on the brightness.

Another important parameter is then the source size. The smaller source size, the smaller electron probe can be achieved [1].

Moreover, the smaller source size leads to higher partial spatial coherence. This leads to the next significant parameter, which is the coherence of the electron beam. It influences the resolution and contrast that can be achieved. The energy spread of the source associates with this parameter too, because it defines the partial temporal coherence [1].

The energy spread and the effect of source size are described by certain characteristics which are more described in the section Source effect.

So that, in the case of STEM are required these parameters: high brightness, small source size with small energy spread and thus high beam coherence. It corresponds to the FEG (especially CFEG) sources, which are the best and essential choice of the electron source in this case [1].

1.4 Electron lens

The electrons could be focused by electrostatics or electromagnetics lenses. However, in the case of STEM (or TEM) the electromagnetic lenses are used, because this type of electron microscope uses too high acceleration voltage. The usage of electrostatic lenses for TEM brings some complication [26][7].

Both of these types of lenses works similar as a glass lenses which means that they deviate the trajectory of the electrons that are emitted from a source. This deviation finally causes the convergence of these electrons to a single focal point. Furthermore, electron lenses are controlled by amount of current that passes through them. This enables us to modify their magnification [26][7].

The field that is produced by the lenses must be radially symmetric as possible. So that they have to be manufactured well, because manufacture imperfections can lead distortions in the symmetry. Nevertheless if the field is symmetrical, the aberrations are symmetrical too. These aberrations have significant influence to whole STEM imaging.

The simplest electromagnetic lens is similar to a solenoid. Inside of this there is a magnetic field, which is not perfectly homogeneous and thus it causes aberrations that are identical to optical lens aberrations [26][7].

2 IMAGING ABERRATIONS

The specimen is located in the magnetic field that is formed by the pre-field and post-field of the objective lens. To make it easier, we can treat the pre-field and post-field separately. In the case of STEM, the pre-field of objective lens is more important, because it focuses the electron beam onto the specimen plane. The focused electron beam is called the electron probe, which represents a demagnified image of the electron source. The both, the specimen plane and the electron probe are situated in the back focal plane of the pre-field of objective lens. However, the probe is not perfect. In ideal world, it would be stigmatic, but in practice it is not. There are several factors that influence the forming of electron probe and thus the information transfer in STEM imaging. These are the effect of the finite aperture, the lens aberrations and influence of the electron source.

First, we individually describe them from a geometrical point of view to better understanding of them. However, it is necessary to describe them also from a wave optical point of view, because this approach finally allows us to describe the electron probe as a combination of all effects that influence its forming.

2.1 Aperture effect – diffraction limit

Geometrical consideration

In this case, the influencing factor is the present of the illumination aperture. This component controls the illumination (convergence) angle and thus it restricts the angular range of the illuminating electrons that form the electron probe. So that it controls the size of the electron probe.

When we consider that the aperture is approximately illuminated by a parallel beam, we will get an Airy-pattern-type electron probe. Since this aperture is needed the Airy pattern is unavoidable.

The central maximum of the Airy pattern is dominant and around that there are side lobes that have significantly lower intensity. The radius of diffraction-limited probe δ_D is considered as the first zero intensity of the Airy pattern.

$$\delta_D = 0{,}61\frac{\lambda}{\alpha} \tag{2.1}$$

λ is the electron wavelength. α is the illumination (convergence) semi-angle, which is defined by the aperture opening [8].

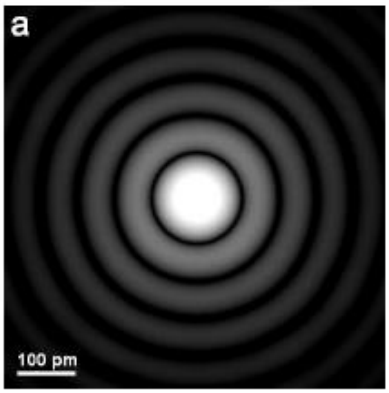

Figure 2.1: Airy pattern [8]

From this equation of Rayleigh criterion, the width of the electron probe increases with increasing wavelength and decreasing illumination angle. So that, when we have infinite illumination angle and wavelength that goes to zero, the δ_D would be zero too and the electron probe would be point-like. But in real situation, the illumination aperture has finite size and wavelength of electrons has also several restrictions, especially in the case of biological specimens.

Moreover, if δ_D is zero, the total beam current would be zero too – more detailed described in the section of geometrical source size [8].

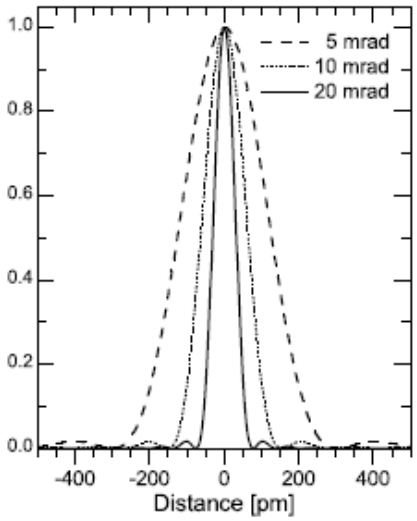

Figure 2.2: The graph shows, that with increasing illumination semi-angle, the central maximum becomes narrower [8].

This restriction of the size of probe due to the illumination angle is called the *diffraction limit.* In this case, when we consider solely limitation by diffraction, the resolution criterion can be then expressed by the Rayleigh limit (criterion) [8].This criterion says that, if two electron probes are close to each other that the maximum of one electron probe overlaps another probe at its first zero, it is the border situation that we can resolve both probes [9].

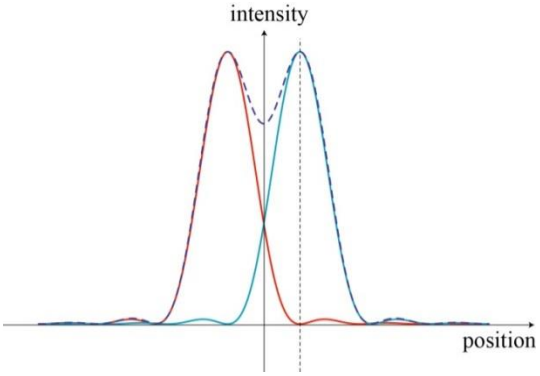

Figure 2.3: Rayleigh limit [32]

Wave optical consideration

Now we derive an electron probe by wave optical description. The electron wave in the aperture plane $\psi(q)$ is focused by the pre-field of the objective lens onto the specimen plane $\psi(r)$. The plane of the illumination aperture and the plane of the objective aperture are aperture planes. They are both described by position coordinate q and the specimen plane is described by the position coordinate r. Let we assume, that the aperture opening is circular and phase and the amplitude of the electron wave are constant across the opening. Then, the electron wave in the aperture plane $\psi(q)$ could be described as a top-hat function.

$$\psi_0(\boldsymbol{q}) = \begin{cases} 1 & if\ |\boldsymbol{q}| < |\boldsymbol{q}_a| \\ 0 & otherwise \end{cases} \tag{2.2}$$

This function can be then approximately described the Fermi function.

$$\psi_0(\boldsymbol{q}) = \frac{1}{1 + exp\left\{\frac{|\boldsymbol{q}|^2 - |\boldsymbol{q}_a|^2}{\delta_a^2}\right\}} \tag{2.3}$$

The radius of the aperture opening is denoted by q_a and it is related to the illumination angle by $\alpha = q_a \lambda$. δ_a is a small fraction of the aperture radius.

For $\delta_a \rightarrow 0$, (2.3) is equivalent to (2.2) and for arbitrarily small but finite values of q_a, the edge of the top-hat function defined in (2.2) is rounded. Furthermore, a non-sharp edge decreases the risk of introducing sampling artifacts in numerical methods [8].

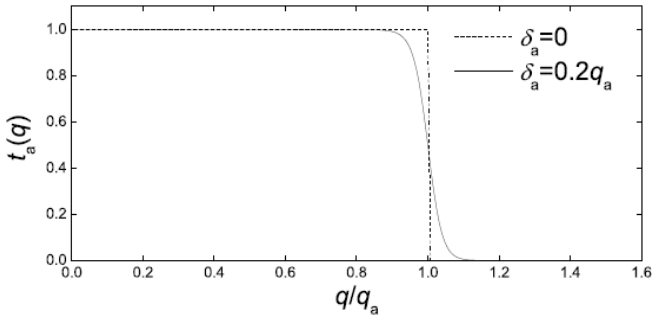

Figure 2.4: Fermi function [10]

In STEM, the specimen plane is conjugate to the plane of the electron source and thus the electron wave in the aperture plane linked to the electron wave in the specimen plane. This connection is given by a Fourier transform. So that, we could then simply do the Fourier transform of the Fermi function, which represents approximation of the electron wave in the aperture plane $\psi(q)$ and we obtain the electron wave on the specimen plane $\psi(r)$. This electron wave then corresponds to the diffraction-limited electron probe which is an Airy-pattern-type electron probe [8].

Of course, it is clear also from signal theory, that the Fourier transform of top hat function is the *Sinc* function, that is similar to the Airy-pattern [11].

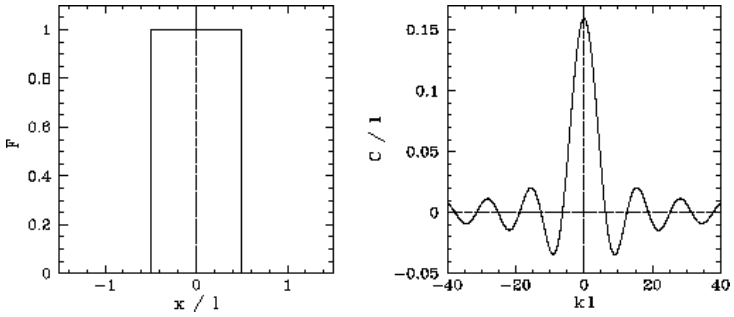

Figure 2.5: Fourier transform of rectangle function [12]

2.2 Electron lens effect

In the previous section, we discussed the impact of the diffraction limit on the forming of an electron probe. However, this is not the only contribution that affects the electron probe. If it was, we would simply set the largest illumination aperture in order to obtain the smallest probe. Due to the fact that electron lenses are not perfect, we have to consider also a contribution of their aberrations to the forming of an electron probe.

Moreover, the Scherzer´s theorem also recommends to take this fact in to account. It states that in stationary electromagnetic lenses, that are rotationally symmetric, the

both constants of spherical and chromatic aberration are always finite and positive. So that their affect is unavoidable [8].

2.2.1 Defocus and spherical aberration

Geometrical consideration

This effect of objective lens is described by the constant of spherical aberration C_3 and by the defocus C_1. While C_3 is a fixed characteristic of the lens, the parameter C_1 is variable and its choice can affect the rate of impact of spherical aberration. So that, C_1 can be adjusted and C_3 represents the actual limit.

Let we consider that, electron probe is formed from a point-like electron source. Then, if we have an ideal lens, all the rays coming from the point-like source are formed in one single point in the image plane. However, in the case of real lens, the effect of positive spherical aberration occurs. It means that, the rays that pass the lens in a certain distance from the optical axis are brought more and they focus closer to the lens than rays that run near the optical axis. In other words, the focal distance of the lens decreases with increasing distance from the central axis [8].

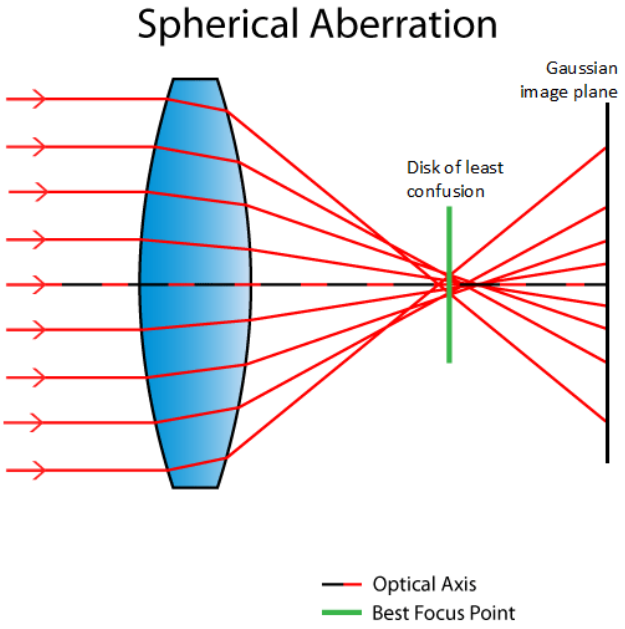

Figure 2.6: Spherical aberration [13]

In the focal distance, for the rays that run through the lens very near to the optical axis, there is located the Gaussian focal plane. If the lens is ideal, all the rays focus there

in single point. However, there is a broad disc instead of a point-like image. One should assume that, the specimen is situated here, but there is a better place. Between the lens and the Gaussian focal plane, there is an area where the envelope of all the rays forms another disk that is significantly smaller than the disk in the Gaussian focal plane. This disk is called the *disk of least confusion* and it also represents the smallest possible electron probe that could be achieved with the limitation of spherical aberration.

$$\delta_S = \frac{1}{4} C_3 \alpha^3 \tag{2.4}$$

Moreover, this equation shows that the spherical-aberration-limited probe size depends also on a given illumination semi-angle. It may seem that the smaller the illumination semi-angle leads to the smaller radius as it goes in the case of diffraction limit. However, it is apparently opposite.

The defocus C_1 describes the deviation of the focus from the Gaussian focal plane. It moves with the disk of least confusion on the central axis, so that its value should be finite. Furthermore, his proper adjustment can be then used to minimize the effect of spherical aberration [8].

There are two ways to improve the resolution relative to spherical aberration: reduction of C_3 or increase of accelerating voltage and thus decrease of λ. Accelerating voltage has a restriction due to radiation damage of a specimen by high energy electrons. The reduction of C_3 can be achieved by the corrector of spherical aberration, which is located in front of the objective lens in STEM and it then allows to decrease the probe size [1].

Wave optical consideration

Let we look at the spherical aberration in the wave optical point of view. Lens aberrations are in this case considered as the phase shifts in the aperture plane. So that, defocus C_1 and spherical aberration C_3 are described in the aperture plane and thus they are also called aperture aberrations. They are described by the aberration function, which describes changes of the phase of the electron wave in the aperture plane.

$$\chi(\boldsymbol{q}) = \chi(q) = \frac{1}{2} q^2 \lambda^2 C_1 + \frac{1}{4} q^4 \lambda^4 C_3 \tag{2.5}$$

We assume that the aberrations are isotropic, so that we can switch to the scalar notation. We than adjust a general wave function $\psi_0 = A \cdot exp\{iB\}$ to our purpose. We modify the amplitude by the aperture function mentioned above. Then we modify

the express of the phase by the aberration function. Thus, we incorporate the effect of the lens aberrations into the probe calculation.

$$\psi_0(\boldsymbol{q}) = \frac{1}{1+exp\left\{\frac{|\boldsymbol{q}|^2-|\boldsymbol{q}_a|^2}{\delta_a^2}\right\}} exp\left\{-\frac{2\pi i}{\boldsymbol{\lambda}}\chi(\boldsymbol{q})\right\} \tag{2.6}$$

So that, the first part of this equation determines the amplitude of the wave function in the aperture plane and the second part represents the phase. Indeed, this equation covers the contribution of the aperture and the contribution of the aperture aberration to the wave function. In a next step, we simply take the Fourier transform of this equation of the electron wave in the aperture plane and we obtain the coherent electron wave on the specimen plane.

$$\psi_0(\boldsymbol{r}) = \int_{-\infty}^{\infty} \frac{exp\left\{-\frac{2\pi i}{\lambda}\chi(q)\right\}}{1+exp\left\{\frac{|\boldsymbol{q}|^2-|\boldsymbol{q}_a|^2}{\delta_a^2}\right\}} exp\{-2\pi i\boldsymbol{q}\cdot\boldsymbol{r}\}d\boldsymbol{q} \tag{2.7}$$

The integral is calculated within aperture opening, therefore between values q_a. Moreover, if the specific position r_p needs to be calculated, r can be replaced by r-r_p. Finaly, when we take the modulus of this complex wave function $\psi_0(r)$, we obtain the intensity $I_0(r)$ of the electron probe on the specimen plane [8].

$$I_0(\boldsymbol{r}) = \psi_0(\boldsymbol{r})\bar{\psi}_0(\boldsymbol{r}) = |\psi_0(\boldsymbol{r})|^2 \tag{2.8}$$

2.2.2 Chromatic aberration – partial temporal coherence

Geometrical consideration

The problem of partial temporal coherence consists of two parts: non-monochromatic electron emission and undesirable lens property – chromatic aberration. If we had an ideal electron source that emits electrons of equal energy, we may do not have to a problem with the chromatic aberration. However, real electron sources emit electrons with certain energy spread ΔE that has characteristic energy distribution. We can approximate this distribution with Gauss function.

Another problem is that, electron lenses are not achromatic – they suffer from chromatic aberration C_c. This means that, the focal point of the lens depend on the energy of the electrons. When we have electrons with the nominal electron energy E_0, their focal plane lies in the Gaussian focal plane. However, electrons that have lower

energy than the nominal energy have their focal plane in front of the Gaussian focal plane. On the other hand electrons of energies greater than E_0 have a focal point behind. Hence, when we have a point-like electron source, the electron probe is not a point but it is formed to a disc of confusion in the Gaussian focal plane. The radius of the disc of confusion due to the chromatic aberration is given by:

$$\delta_C = C_C \alpha \frac{\Delta E}{E_0} \tag{2.9}$$

This equation shows that, the size of this disk proportionately increases with width of the energy spread. Furthermore, with decreasing opening angle of the aperture and thus increasing illumination semi-angle, the diameter of the disk decreases [8].

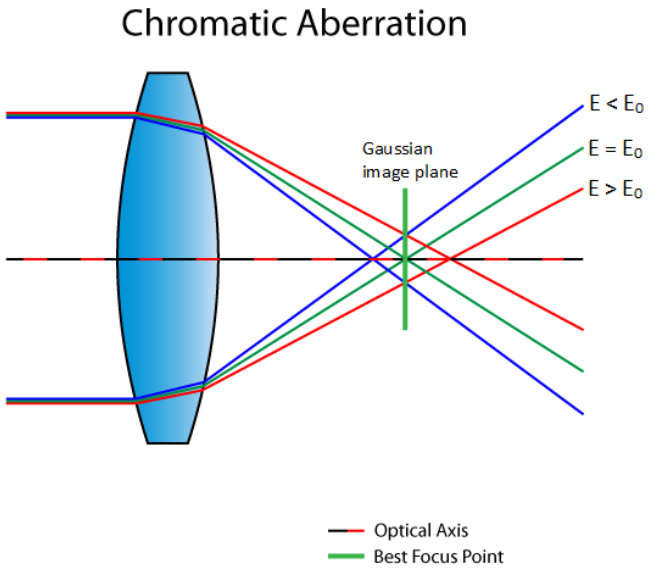

Figure 2.7: Chromatic aberration [14]

Moreover, the total energy dispertion of electrons is given by several contributions: initial dispersion δ_E, fluctuation of accelerating voltage ΔV, fluctuation of exciting current of the objective lens ΔI. Moreover, the loss of energy of electrons due to trasmission through the specimen are insignificant in the case of STEM.

$$\Delta f = C_C \left[\left(\frac{\Delta V}{V} \right)^2 + \left(\frac{2\Delta I}{I} \right)^2 + \left(\frac{\Delta E}{E_0} \right)^2 \right]^{1/2} \tag{2.10}$$

However, nowdays, these parameters are at high level, so that the impact of chromatic aberation due to them is small. Moreover, there can be used also an electron monochromator, which significantly reduce the width of the beam [1].

Wave optical consideration

The combination of finite energy spread of the electron emission and the chromatic aberration of the lens leads to a finite spread of focus. Because of the variation of electron energies δE, the chromatic aberration C_C actually causes a variation of the defocus δC_1.

$$\delta C_1 = C_C(E - E_0)/E_0 = C_C \delta E/E_0 \tag{2.11}$$

So that, this means that the focus is blurred. This spread of the defocus has to be incorporated to the calculation of an electron probe. This incorporation is realized by the aberration function χ, which is incorporated in the wave function $\psi(r)$, mentioned above in the section of spherical aberration. This function χ is a function of defocus C1 and we replace this single value with the spread of defocus δC_1. The defocus distribution $T(C_1)$ depends on the energy distribution T(E), which assume that it is a Gaussian function. The electron probe can be than calculated by this adjusted equation.

$$I_0(\boldsymbol{r}) = \int_{-\infty}^{\infty} [|\psi_0(\boldsymbol{r}, E)|^2] T(E) dE \tag{2.12}$$

This equation shows, that the wave function $\psi(r;E)$ is further depend on the energy E, which is given by energy spread δE. So that, we have to calculate an electron probe $\psi(r;E)$ for each energy E within the δE. This means that the final intensity of the electron probe is the superposition of electron probes, weighted by T(E), respectively $T(C_1)$. Due to, this superposition is incoherent [8].

2.2.3 Other lens aberrations

In this section, there are described other lens aberrations that are less significant that these mentioned above, but they are still present. These are astigmatism and coma, which are also called defects of adjustment, because they can be commonly treated.

Astigmatism

Astigmatism is an aberration that causes the focus length of the lens changes its size in dependence of an azimuth of the lens. So that, the focus length is different for two rays which go through the lens in two perpendicular planes. The astigmatic difference is then the distance between these focuses. Causes of the astigmatism are different: elipticity of openings of the pole extensions**,** radial shift between the pole extensions and apertures, non-homogenous material of the pole extensions**.** Astigmatism can be caused also by a specimen, especially if it is an ferromagnetic material.

At the atomic resolution, even weak astigmatism can distort an image by an elliptical interference. Strong astigmatism then prohibits whole imaging. Moreover, astigmatism needs to be watched, because it can change its character during the acquisition due to a contamination of a specimen, change of place of an observation or when the specimen is rotated.

This aberration can be treated by component called stigmator, that produce an eliptic-symetrized magnetic field, that is superposed to the astigmatised beam [1].

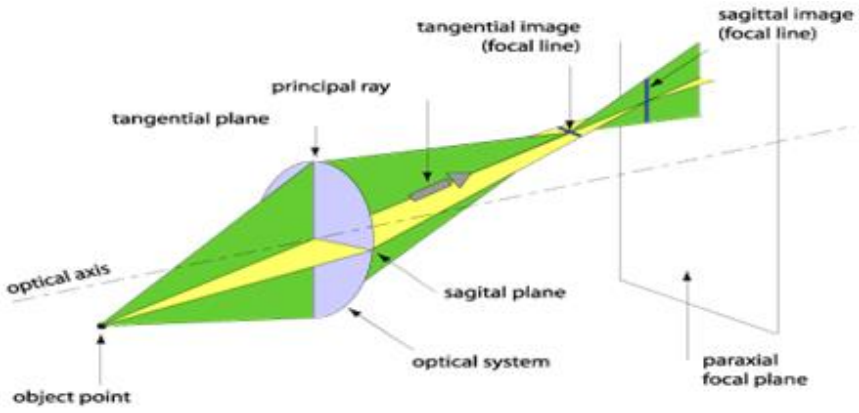

Figure 2.8: Astigmatism [15]

Coma (asymmetrical aberration)

This aberration means that, if the specimen is illuminated askew relative to perpendicular optical axis, the circular-symetised electron probe is deformed to a spot, that could be assigned to a comet. Although, this aberration is not so important as i.e. spherical aberration, its influence could be significant at the atomic resolution. When the primary electron beam is slanting relative to optical axis of objective lens, the diffracted beams has different phase shifts and because of that the contrast decreases.

Principle of correction is based on the fact that this distortion of the probe is depended on the angle of the slant. It is done by deflection coils for coma correction. However, the correction is just partial, because of its negative influence to spherical aberration [1].

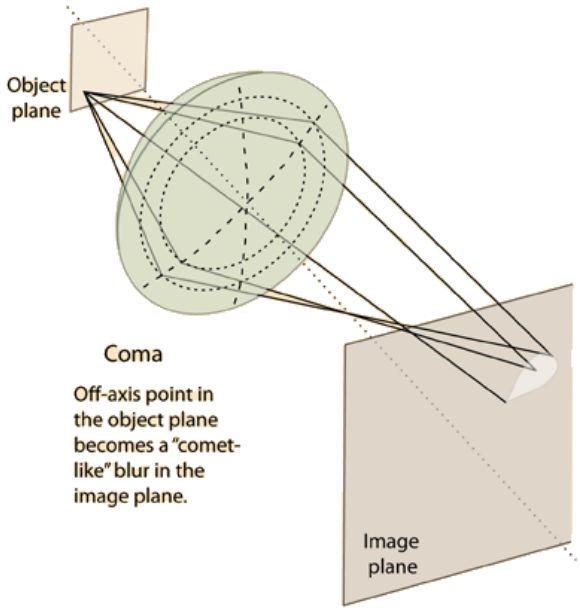

Figure 2.9: Coma [30]

2.3 Electron source effect

2.3.1 Effect of the source size – partial spatial coherence

Geometrical consideration

In the previous sections, we assume a point-like electron source. However, real electron sources have finite size, so that the image of the electron source, thus the electron probe can never be point-like. Maybe, when we demagnify this image of electron source, the electron probe can be point-like. However this would lead to an electron probe of zero current I_{probe}. Nevertheless, the way of the demagnification is possible, but it has restrictions. We can approximate this situation that we demagnify the source of area A_S to a circular area of radius r_{geo} ($\pi^2 \, r_{geo}^{\,2} = M \, A_S$, where M is (de-)magnification). From the definition of the brightness B in the section of electron sources, we can derive an equation of the probe current I_{probe}.

$$B = \frac{I_s}{\Omega A_s} = \frac{I_{probe}}{\pi \alpha^2 A_s} \tag{2.13}$$

$$I_{probe} = B \frac{\pi^2 \alpha^2 r_{geo}^2}{M} \tag{2.14}$$

It is clear that I_{probe} linearly depend on brightness B as well as the source size A_S and α. If we apply a high demagnification for a given illumination angle α, the $r_{geo} \rightarrow 0$ and the source will be point-like. However I_{probe} will be zero too. But if would exist the source that has $B = \infty$, this way would be possible. So that, demagnification comes at the expense of beam current. We can conclude that electron sources of high brightness are very important for STEM. The higher the brightness of the source leads to higher the current I_{probe} that can be achieved at sufficiently small size of an electron probe.
Moreover, the source size is independent of how many lenses are between source and specimen. So that it is also independent of lens aberrations and of the diffraction limit [8].

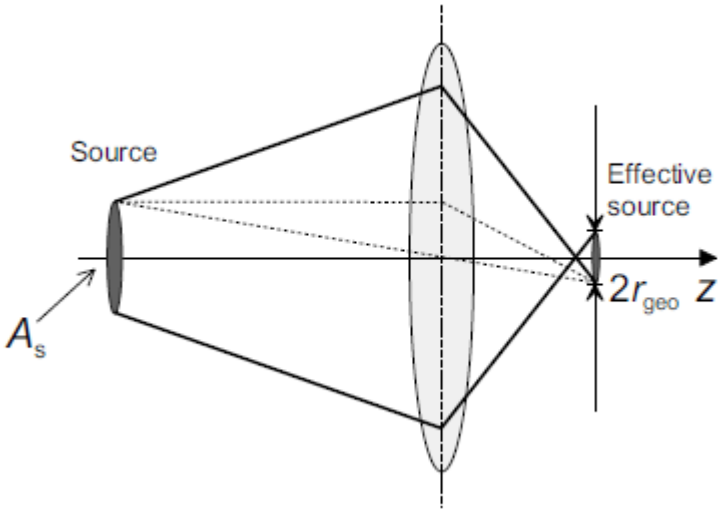

Figure 2.10: Demagnification of the source of area As to an effective source of radius r_{geo} [8]

Wave optical consideration

If we know, that the electron source is not point-like, we would incorporate this fact into the calculation of the electron probe from a point of view of wave optics. In the description before, we approximate the electron source as a circular surface with homogenous electron emission. However, real electron sources are not disk-like and their emission of electrons is not homogenous. They have an emission characteristic called a source intensity distribution function S(r). This describes the distribution of the emitting points of the source that are projected and demagnified onto the object plane. For our purposes, we can approximate this function by Gaussian function.

From these arguments, we can conclude that the electron beam does not emitted from a single point of an electron source, but it is emitted from a multitude of points described by S(r). These emitting points then contribute to the electron probe, so that each element of the source produce a coherent electron probe as described in the previous sections, where we assumed a point-like source. Thus obtained probes then lead to obtain a final probe. However, the combination of these probes is incoherent due to non-homogeous distribution S(r).

Hence, in order to incorporate the source intensity distribution S(r) to calculation of the probe we have to convolute the equation of the coherent probe wave field with the source intensity distribution S(r).

$$I_0(\boldsymbol{r}) = |\psi_0(\boldsymbol{r})|^2 \otimes S(\boldsymbol{r}) \tag{2.15}$$

This adjustment essentially reduces the transfer function at high spatial frequencies. In other words this operation leads to an incoherent blurring of the electron probe.

Moreover, because this source effect is an incoherent contribution, we do not assume any interference between electrons emitted from different points of the source. So that, we then deal only with the intensity of the electron probe, not with its phase and we also.

So that, before, we assumed a fully coherent electron probe and now, after this incorporation, we take in to account the limitation of the electron beam coherence. Indeed, this effect of the finite source size is also called partial spatial coherence [8].

2.3.2 Energy spread of electron source

The real sources are non-monochromatic, which means that they do not emit electrons of one single energy, but they emit them in a certain energy spread around nominal energy E_0. This energy spread is further described by energy distribution function, which is characteristic for given electron source. We can approximate this distribution with Gauss function around a nominal energy $E_0 = eU$. However, this model does not take into account the emission characteristics for a given electron source, but for our purpose it is sufficient. This fact is mainly associated with chromatic aberration of the objective lens and it leads to problem of partial temporal coherence. This problem is more detailed described in the section of chromatic aberration, including this energy spread [8].

2.4 Combined effect of the imaging aberrations

In order to describe the combined effect of the aberrations mentioned above, we have to do it in a point of view of wave optics. We combine only main aberrations because we suppose that other aberrations are insignificant.

We add the aberrations step by step in to the calculation of the electron probe. First, we start with influence of the illumination aperture in front of the specimen. This component restricts the incident electron beam by the illumination angle, which is given by the circular aperture opening. So that, the electron wave in the aperture plane is a top-hat function, which can be approximated by the Fermi function [8].

$$\psi_0(\boldsymbol{q}) = \frac{1}{1 + exp\left\{\frac{|\boldsymbol{q}|^2 - |\boldsymbol{q}_a|^2}{\delta_a^2}\right\}} \tag{2.3}$$

After that, we can add the influence of defocus and spherical aberration that are described by the aberration function χ, also in the aperture plane. We then incorporate this aberration function and the aperture function into a general wave function $\psi_0 = A \cdot exp\{iB\}$. We get the wave function in the aperture plane that covers the contribution of the illumination aperture with the defocus and spherical aberration, thus the all coherent contributions.

$$\psi_0(\boldsymbol{q}) = exp\left\{-\frac{2\pi i}{\lambda}\chi(\boldsymbol{q})\right\} \frac{1}{1+exp\left\{\frac{|\boldsymbol{q}|^2-|\boldsymbol{q}_a|^2}{\delta_a^2}\right\}} \tag{2.6}$$

In order to obtain the intensity of the electron probe in the specimen plane, we take the Fourier transform of the equation above and after that we take the modulus of that

$$I_0(\boldsymbol{r}) = \psi_0(\boldsymbol{r})\bar{\psi}_0(\boldsymbol{r}) = |\psi_0(\boldsymbol{r})|^2 \tag{2.8}$$

In the calculations above, we still assume the point-like electron source. Now we incorporate the impact of the real non-point-like electron source, which is described by the non-homogenous intensity distribution function S(r). This describes a multitude of source emitting point. Each point produce an electron probe as described above, i.e. point-like-captured electron probe. All these probes are then non-homogenously combined into a final electron probes. So that, this is an incoherent contribution to the electron probe. We can incorporate it into the calculation as a convolution between the intensity distribution function S(r) and the intensity of the coherent probe wave field $I_0(r)$ [8].

$$I_0(\boldsymbol{r}) = |\psi_0(\boldsymbol{r})|^2 \otimes S(\boldsymbol{r}) \tag{2.15}$$

Finally, we incorporate an impact of partial temporal coherence, which is given by the chromatic aberration of the objective lens and by the energy spread of the source δE, which is described by non-homogenous energy distribution T(E) of the electron beam. This influence essentially causes a non-homogenous spread of defocus δC_1, which has to be incorporated to the aberration function χ, that we incorporate to the calculation at the beginning. This means that, the coherent electron wave $I_0(r,E)$ on the specimen plane is dependent also on the energy E within δE. So that, we have to calculate all probes for all energies and then summarize them into a final probe simultaneously with weightening by T(E) of T(C_1) respectively. So that, we talk about the incoherent superposition of electron probes, that is given by this equation

$$I_0(\boldsymbol{r}) = \int_{-\infty}^{\infty} [|\psi_0(\boldsymbol{r}, E)|^2 \otimes S(\boldsymbol{r})] T(E) dE \tag{2.16}$$

Due to introduction of partial temporal and spatial coherence to the calculation, the final transfer function is essentially reduced at high spatial frequencies. This final equation of the intensity of the electron probe in the specimen plane covers all the significant coherent and incoherent contributions to the electron probe. Because it represents the combinations of these contributions, we can use it as a basic model of distortion of the electron probe in STEM systems [8].

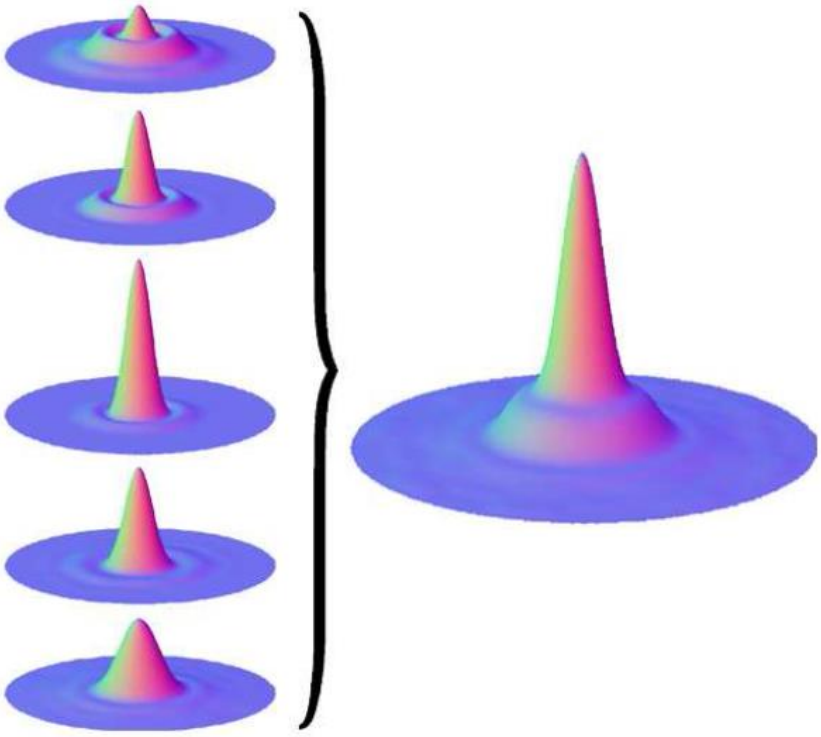

Figure 2.11: Final from of the electron probe [8]

2.5 Other interference

In addition to the influence of the objective lens, the electron source, and the illumination aperture, there are other factors that can affect STEM imaging. It can be for example, the detector dark noise or other noise from the environment, which may be either electromagnetic or mechanical in nature. Electromagnetic noise may result, for example, from the instability of the lens or the detector. Mechanical instability may be due to an unstable specimen holder or thermal motion of the specimen. If this interference is high frequency, it is difficult to detect and can cause the probe size to increase. However, if its frequency is lower, it can be more easily detected by Fourier Transform [8].

The character of the noise may be of a different nature, but predominantly it is the Posson's noise [16].

Additionally, the quality of the STEM imaging can be affected by inaccuracy of raster scanning that is inversely proportional to the scanning speed [17].

2.6 Imaging aberrations summary

Now we conclude the all main contributions mentioned above. We assume that the astigmatism and coma are sufficiently small and they do not affect the imaging process significantly. First we take a look at the contributions independently and we consider their impacts from a point of view of geometry. However in order to understand the impacts of these contributions more clearly, then we evaluate them from a point of view of wave optics.

Geometrical consideration

The crucial limitation in the resolution of STEM imaging is the electron probe size, because when two objects are at the smaller distance then the probe size, they cannot be detected. So that, a smaller size of electron probe means higher resolution, that is the general fact. In order to obtain the smallest possible probe, the probe-limiting factors have to be balanced to their minimal impact [8].

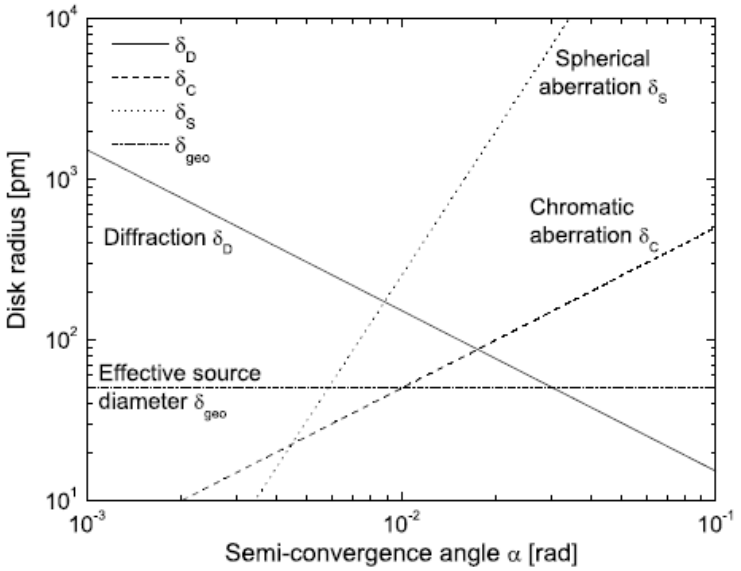

Figure 2.12: Contributions to the STEM probe and their dependency of the diffraction limit [8]

From the plot it is clear, that influence of the chromatic aberration is not critical. However, it is also clear that the diffraction limit and the spherical aberration are the most limiting factors and they need to be considered and balanced.

The Scherzer incoherent conditions solved this problem. They derived the optimum defocus and the optimum illumination semi-angle for given C_3 and λ, that allow to achieve the highest possible resolution (the smallest possible probe size) in regard to spherical aberration.

$$C_{1\,opt} = -\sqrt{\lambda C_3} \tag{2.17}$$

$$\alpha_{opt} = \left(\frac{4\lambda}{C_3}\right)^{\frac{1}{4}} \tag{2.18}$$

Wave optical consideration

However, in order to better understand the electron probe, it is necessary to use the point of view of wave optics, because it allows us to see the electron probe as result of the collective effect of image aberration mentioned. Finally, it also allows to consider the probe as 3D intensity distribution, which describes the lateral and longitudinal extension of the electron probe.

The lateral extension determines the lateral resolution of STEM and the longitudinal determines the depth of field and thus the depth resolution along the optical axis [8].

The depth of field is determined by the aperture opening and thus by the illumination angle. The depth of field is usually larger than the thickness of the specimen, so that the whole 3D information in the specimen is then summarized. If we increase the illumination angle, the depth of field becomes smaller. However, this is restricted by Scherzer incoherent conditions and thus the spherical aberration. So that, when we use a spherical aberration correction, then than the illumination angle can be larger and we can obtain smaller depth of field

The partial temporal coherence and thus the chromatic aberration influence the electron probe in both extensions. However it is not probe size limiting factor, as it is expected in the section of geometrical considerations.

The electron probe is limited mainly by spherical aberration that influences the defocus and the aperture opening from point of view of Scherzer incoherent conditions.

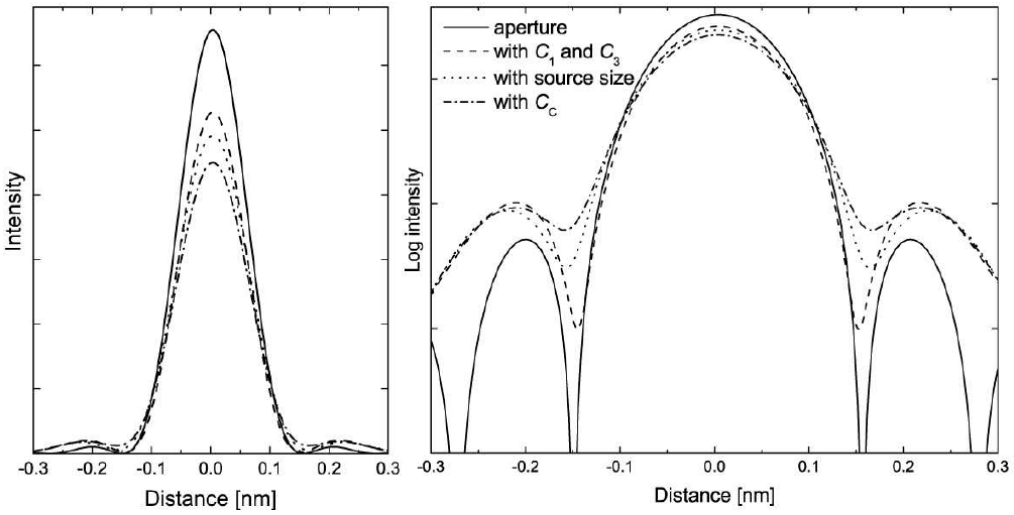

Figure 2.13: Electron probe intensity profiles. Acquisition parameters are common and realistic except the chromatic aberration – here, it is too high in order to better displaying of that, because its influence is small. [8]

In this figure there are stepwise illustrated all impacts of the individual contributions to the probe. The left figure represents normalized intensity of the electron probe, calculated by (2.16). The right figure represents the same, but in logarithmic scale for display a detail.

It is also clear that the intensity of central maximum gradually decreases, but none of the contributions significantly increases the width of central maximum. The resolution can be then determined nearly by the diffraction limit α_{opt}. However, if the intensity of the central maximum decreases, the lost intensity is transferred to side lobes. So that the main impact of the is increase of the intensity of side lobes of the probe, even if the Scherzer incoherent conditions are fulfilled. However the higher background intensity causes decrease of image contrast [8].

3 AQUSITION PARAMETERS

For given electron microscope, there are certain fixed parameters that are given by the electron source and the objective lens that are used.

The objective lens has two main parameters: the constant of spherical aberration C_3 and the constant of chromatic aberration C_C. These constants are fixed for given objective lens.

The electron source is described by two main characteristics: the energy distribution function T(E) and the source intensity distribution function S(r). These characteristics are also fixed for given electron source.

The only parameter that is variable and independent of used components is the wavelength. However, the variability of this parameter is restricted too, mainly in the case of biological specimens.

Other parameters that are given by these main parameters are the illumination semi-angle, the defocus and the spread of the defocus. The first two parameters are given by the Scherzer incoherent conditions that depend on λ and C_3. The spread of the defocus is then given by the chromatic aberration C_C of the objective lens and by the energy distribution function T(E) of the electron source.

So that, the electron source and the objective lens that is used then determine the forming of the smallest achievable electron probe and thus the best achievable resolution and contrast. This means that the right choice of these two components is very important. However, the most limiting factor is the spherical aberration. Nevertheless, there is a correction of this aberration. It is quite expensive, but using it the resolution grow in both extensions. The chromatic aberration can be corrected too, but its impact is not as crucial as the impact of spherical aberration.

Moreover, when an image is scanned, other important parameters are the dwell time and magnification. Dwell time mainly affects the quality of information. The longer the electron probe stays at a certain location, the more signal we receive and thus the higher SNR. The magnification mainly affects influence of aberrations to the image. This is given by the scan step that determines the distance between the electron probes at time t_i and t_{i+1}.

4 RESTORATION PROCESS

4.1 Distortion model

When we measure an input signal (image) *f(x)* using a system (device) that is defined by the impulse characteristics *h(x)*, we get the output signal (image) *g(x)*. This output image partly corresponds to the original input image, but it is distorted when it passes through the measurement system [18].

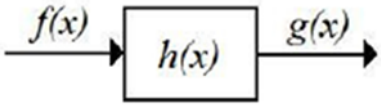

$$g(x) = f(x) * h(x) \tag{4.1}$$

The resulting image is thus given by the convolution of the input signal with the impulse characteristic of the system. This would be an ideal case. In the real system, however, there is always noise *v(x)*, most often additive noise. The resulting distortion model will then take the following form:

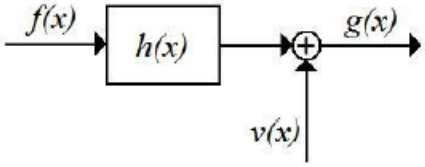

$$g(x) = f(x) * h(x) + v(x) \tag{4.2}$$

So we get a signal at the output that will always be different from the original one. The size of this difference always depends on the characteristics of the system and on the noise level [18].

Most often distortion models are additive Gaussian noise or Poisson noise.
Gaussian noise model is approximated by Gaussian layout. A two dimensional random variable with a Gaussian normal distribution has a probability density given by:

$$p(f) = \prod_{m,n} \frac{1}{\sigma_f \sqrt{2\pi}} e^{\frac{f^2(m,n)}{2\sigma_f^2}} \tag{4.3}$$

where σ_f is the standard deviation.

Poisson's noise model corresponds to the quantum nature of light. Its distribution is given by:

$$p(N) = \prod_{i=1}^{M} \frac{\mu^N \exp(-\mu)}{N!} \tag{4.4}$$

where *N* is the number of photons detected and μ is deviation. However, this noise is not additive [19].

4.2 Pont spread function (PSF)

In the previous distortion model, it was mentioned that the distortion is given by the impulse characteristic *h(x),* which is in this case often referred as the point spread function (PSF).

The PSF of the optical device is an image of a single point of the object, so it is basically a 2D impulse characteristic of the system. The level of blur in the image of this point is a measure of the quality of the optical system.

In our case, we consider the PSF as the wave function of an electron probe derived on the basis of wave optics.

$$I_0(\boldsymbol{r}) = \int_{-\infty}^{\infty} [|\psi_0(\boldsymbol{r}, E)|^2 \otimes S(\boldsymbol{r})] T(E) dE \tag{2.16}$$

This feature includes all the important contributions that participate in forming the final electron probe. Less significant effects have been neglected for the sake of simplification. The spatial variation of this function has also been neglected. This is due to the aberration called the coma, but it should be sufficiently corrected. This step will greatly facilitate the next implementation. However, if this simplification will have too much impact on the final result, this spatial variation will have to be included in the calculation [20].

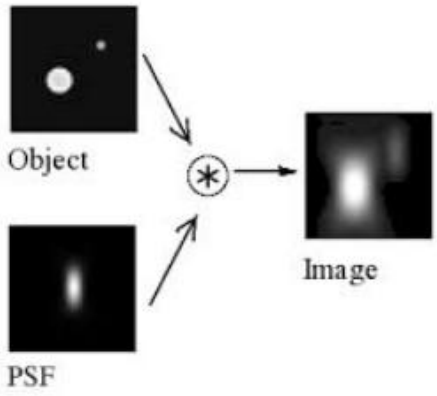

Figure 4.1: Point spread function [20]

4.3 Non-blind deconvolution methods

Deconvolution aims to restore the distorted and noised image *g(m,n)* in order to look like the original image *f(m,n)*. There is a large number of individual deconvolution methods, but they are generally divided into two groups: non-blind deconvolution and blind deconvolution. The non-blind deconvolution is based on the assumption that we know the PSF of the system that negatively affects the acquired signal. This can be determined either by calculation using the theoretical model of the given system or by measuring the pre-known input signal.

On the other hand, the blind deconvolution methods are based on total ignorance of PSF or they only use partial information of PSF that is moreover changed during the calculation [19].

The aim of this thesis is, however, the use of non-blind deconvolution, so we will only deal with these methods.

NEAREST-NEIGHBORS METHODS

These are the basic methods of non-blind deconvolution. They can be classified into two groups: the nearest-neighbors methods and the multineighbors methods. The calculation is simple. The good feature of this method is the speed of processing, but the results that are achieved do not belong to the best quality methods. They are not efficient at removing the noise and introduce structural artifacts. The principle is that, the actual sample is subtracted from two nearest samples that are convolved with PSF.

$$\hat{f}_k(x) = g_k(x) - c[g_{k-1}(x) * h(x) + g_{k+1}(x) * h(x)] \tag{4.5}$$

Where $\hat{f}_k(x)$ is estimating sample, $g_k(x)$ actual sample, $g_{k+1}(x)$ and $g_{k-1}(x)$ are nearest samples and $h(x)$ is PSF [19][21].

NO-NEIGHBORS METHODS

Another simple method is the method of no-neighbors. The algorithm is derived from the nearest-neighbors method. Again, the great advantage of this method is the speed of processing. However, it is applicable only to a limited set of simple signals [19][21].

LINEAR METHODS

These methods also belong to simple deconvolutioin methods. These methods include, for example, inverse filtering, pseudo-inverse filtering, linear least square (LLS) methods and Tikhonov filtering. However, these mentioned methods are based on a distorting model that does not take noise into account. Therefore, they are not very effective in practice, because of significant amplification of noise.

Wienner filtering, on the other hand, takes into account the presence of additive noise. For high SNR, this algorithm gives quite good results, but for low SNR the results are less suitable.

$$M(\omega) = \frac{1}{G(\omega)} \frac{S_{yy}(\omega) - S_{vv}(\omega)}{S_{yy}(\omega)} \tag{4.6}$$

It is essentially the inverse filter (left expression) that is modified by Wienner correction factor (right expression). This prevents unsustainable amplification of some frequencies. $M(\omega)$ is frequency characteristic of Wienner filter, $S_{yy}(\omega)$ is power spectrum of observed signal and $S_{vv}(\omega)$ is power spectrum of noise [18][21].

NONLINEAR METHODS

To solve the problems that occur in linear methods, nonlinear iteration algorithms can be used at the cost of increased computational complexity. These methods include, for example: Janson van Cittert algorighm or non-linear least square method (NLS). However, their performance is not as good as the Iterative Constrained Tikhonov-Miller algorithm (ICTM), whose results are quite good. This algorithm iteratively minimizes the Tikhonov functional [21].

STATISTICAL METHODS

These methods are extremely effective even when the noise in the obtained image is relatively strong. Their noise strategy have is also better than in the previous methods. They are also useful in obtaining certain information that is not captured by microscopic optics. However, they are more complex and computationally more demanding than linear and nonlinear methods.

These methods include, for example: Maximum a posteriori (MAP) method or Maximum likelihood (ML) method (Lucy-Richardson algorithm) [21].

The Lucy-Richardson method was compared with the ITCM method. The ICTM method is based on a convolutional model of distortion with additive Gaussian noise.
The Lucy-Richardson method is the maximum likelihood estimator for the intensity of a Poisson process. However, this method is relatively sensitive to the presence of noise. Therefore, it is suitable to do some pre-processing before using it, for example, Gaussian image filtering. Algorithms were compared on confocal microscope images, where the noise characteristic is better expressed by the Poisson model. The results showed that the performance of the Lucy-Richardson algorithm is much better than that of the ICTM algorithm. The comparison was made on the basis of the MSE and the I-divergence criterion [22].

5 EVALUATION OF DECONVOLUTION RESULTS

First, the evaluation of deconvolution results is performed on a model situation. The classic image of Lena is taken a then it is distorted by the distortion model described above. So that, the original image of Lena is convoluted with our PSF and then the noise is added. After that, certain deconvolution method is used for a distorted image and we get the output image, which should be less distorted and more similar as the original image. So that the output image is then compared with the original image by certain criterion of similarity. Next, input parameters of given deconvolution function is adjusted in order to get the most similar output image as the original image.
When these optimal parameters are obtained this certain deconvolution method can be used to the restoration of given STEM images.

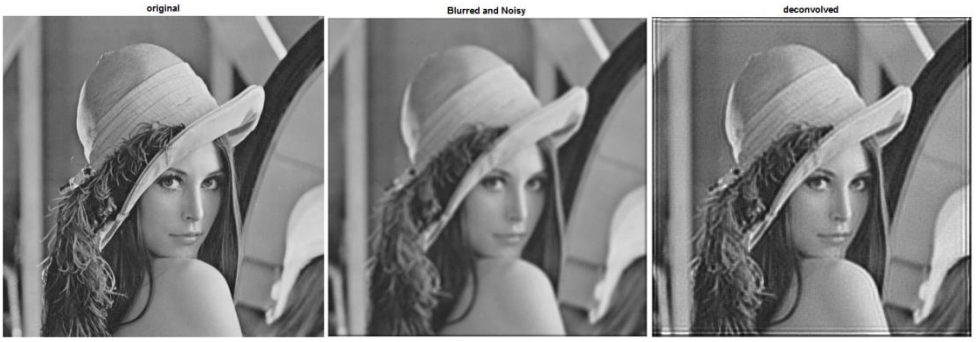

Figure 5.1: Model demonstration of deconvolution

As the criterion of similarity, the RMSE function, the sharpness measure and the comparison of contrast of the images is used.

The root-mean-square error (RMSE) represents the differences between the reference values and the values that are modeled or predicted. In the case of images, this metric means how much two images are similar on a pixel-by-pixel basis. So that, the lower RMSE value means the higher similarity between images.

The formula is:

$$RMSE = \left[\sum_{i=1}^{N}(z_{f_i} - z_{o_i})^2/N\right]^{1/2} \tag{5.1}$$

Where z_{fi} is i-th pixel of input image, z_{oi} is i-th pixel of output image and N is number of pixels [23].

As a sharpness measure, there is used a technique that is based on the frequency domain analysis. This technique provides relatively good results.

The formula is:

$$Image\ Quality\ Measure\ (FM) = \frac{T_H}{M \times N} \tag{5.2}$$

This method takes the maximum value (X) of the amplitude spectrum of given image. This value X than serves as a threshold X/1000. The value T_H is the total number of pixels in the amplitude spectrum, that are higher than given threshold. M x N represents the size of image. The low value of Image Quality Measure (FM) means the higher amount of degradation in the image and thus the poorer the quality of the image. Image Quality measure (FM) where *FM* stands for Frequency Domain Image Blur Measure
The advantage of this technique is that the image quality score always decrease with increasing of blur in the image, in contrast with other popular techniques CPBD and JNB [24].

As a contrast metric, the Histogram Spread (HS) was chosen. This metric is essentially the ratio of the quartile distance to the range of the histogram. Quartile distance is the difference between the 3rd quartile and the 1st quartile. The 1st quartile is the histogram bin at which the cumulative histogram has 25% of its maximum. The 3rd quartile is then the histogram bin at which this histogram has 75% of its maximum. It can be verified that the low contrast images have a low value of HS and for the high contrast images it is vice versa .

The formula is:

$$HS = \frac{Quartile\ distance\ of\ histogram}{Possible\ range\ of\ pixel\ values} = \frac{(3^{rd}\ quartile - 1^{st}\ quartile)\ of\ histogram}{(\max - \min)\ of\ the\ pixel\ value\ range} \tag{5.3}$$

So that, this metric can be used to distinguish between the images which have different contrast level [25].

6 REALISATION

The main aim of this thesis is the definition of the parameter for non-blind deconvolution of images from STEM. The parameter is the PSF of this device. When the parameter is known, the Lucy-Richardson deconvoution method is used to test this postprocessing approach. This method was chosen as the best in the theoretical part of this thesis. On the basis of obtained results, the efficiency of this approach can be determined, relative to case of STEM. Moreover, in order to better utilization of given model, the STEM PSF simulation tool is then created.

6.1 Modelling of the electron probe profile

The non-blind deconvolution approach is strongly depended on precision of given prior information, the PSF. It can be obtained by measuring or by mathematical modelling. This work deals with the second choice of the PSF obtaining. The basis is the Fourier-transform relationship between the electron wave in the aperture plane $\psi_0(q)$ and the electron wave in the specimen plane $\psi_0(r)$ [8].

The aperture plane represents frequency domain, so that this space is reciprocal with reciprocal spatial units q (m^{-1}), which represent spatial frequency. The specimen plane represents original domain with spatial units r (m) [8].

With regard to the assumption of rotational symmetry around optical axis, computations can be simplified to one dimensional case, which represents the profile of given rotationally symmetrical electron wave in given space. Moreover, computational demand significantly decreases.

However, this simplification cannot be used in all computational parts of the algorithm, because then the final results are not sufficiently accurate. This problem mainly concerns the computational part with Fourier transform and thus the modelling of diffraction and spherical aberration. The main reason is that, this computational part represents the interference of electron waves. In real situation, the interference is two-dimensional, so that the final composing of electron waves in the one given point in the specimen plane is influenced by whole space in the aperture plane (influenced by all considered sources of electron waves in this plane). However, when this aperture plane is restricted to one-dimensional profile (e.g. $y = 0$, $x = (-q_a , q_a)$), the influence of the rest of the aperture plane is neglected, so shat the result represents the wave interference only in one cut of the whole space. The result could be mathematically correct, but in

the point of view of physics, this situation is unreal and obtained result is just an approximation of desired result [4].

Nevertheless, after this computational part, the simplification can be used, without any degradation of the quality of the result.

6.1.1 Diffraction

The simplest case of electron probe model is diffraction-limited probe. In this situation, only diffraction restricts forming of electron probe on the specimen plane and other influences are neglected.

This is the case when the calculation using Fourier transform has to be performed in 2D. However, the 1D simplification can be partially used in order to obtain the desired 2D input signal of Fourier transform. First, the profile of the rotationally symmetrical electron wave in the aperture plane has to be obtained. Than the 2D electron wave in the aperture plane is obtained from given electron wave profile. Finally, the 1D profile of the electron wave in the specimen plane is extracted from the two-dimensional result of 2D Fourier transform.

Assuming that, the aperture is circular, the signal (electron wave) in the aperture plane is top-hat function, whose profile is rectangle signal that correspond to the low-pass filter. The cut-off frequency q_a (m^{-1}) of this low-pass filter is given by two acquisition parameters: electron wavelength λ and convergence semi-angle α. In our case, the maximal q_a is $2{,}5 \cdot 10^{10}$ m^{-1}, relative to set of maximal ranges of these two parameters (U_{acc} = 300 kV (λ = 1,97 nm); α = 50 mrad) by $\alpha = q_a \cdot \lambda$. However, it is better to approximate this sharp-edged rectangle signal by Fermi function to avoid possible computational errors, recall to [8].

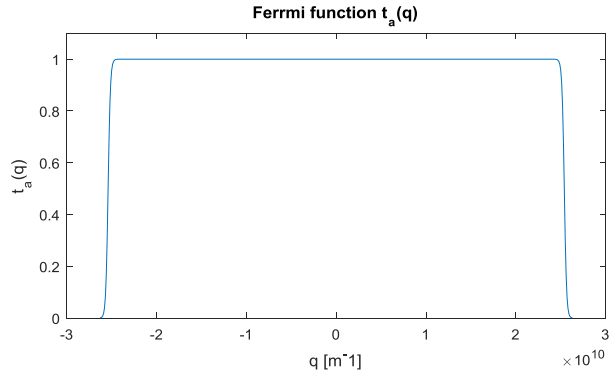

Figure 6.1: Fermi function (*Uacc* = 300 kV, α = 50 mrad, $q_a = 25 \cdot 10^9$)

Minimal sampling frequency F_S was chosen to $1 \cdot 10^{11}$ m^{-1}, which is sufficiently suitable relative to Nyquist theorem ($F_S/2 = 5 \cdot 10^{10}$ $m^{-1} > q_a$) and it gives us sampling period (precision) of $1 \cdot 10^{-11}$ m that is 10 pm. Moreover, there is choice to set the sampling frequency to $1 \cdot 10^{12}$ m^{-1} and resulting precision in original domain would be 1 pm, so that more accurate, but computationally more demanding too [18].

The Ω (sampling step in frequency domain) is set to value of 10^8 m^{-1}. This is the minimal value that can be set, relative to the order of reciprocal values. However, the final result is still accurate enough. Moreover, the calculations are then faster, because Ω influences size of the input matrix of 2D Fourier transform. This is because, to achieve desired sampling frequency, signal length has to be $N = 10^3$ (or 10^4 for $F_S = 1 \cdot 10^{12}$ m^{-1}) by

$$\Omega = \frac{F_S}{N} \tag{6.1}$$

The Ω could be set lower but at the expense of computational demand, while preserving the current accuracy. However, the resulting maximal range in the original domain would be larger. At the Ω of 10^8 m^{-1}, the maximal range in the original domain is 10^{-8} m (10 nm) and thus from -5 to 5 nm, but it is suitable in the case of STEM.
The value of Ω also influences sharpness of transition of the Fermi function. The higher transition sharpness means better approximation of original rectangle profile and it is set by δa. In the case of $\Omega = 10^8$, the δa is set to value of 0,1. At this setting, the sharpness of the Fermi function transition is sufficient. If the transition would be sharper, the transition would be insufficiently sampled and the Fermi approximation of the rectangle function would become rectangle function. In the other hand, the less sharp transition would be sampled better, but final result would be distorted.

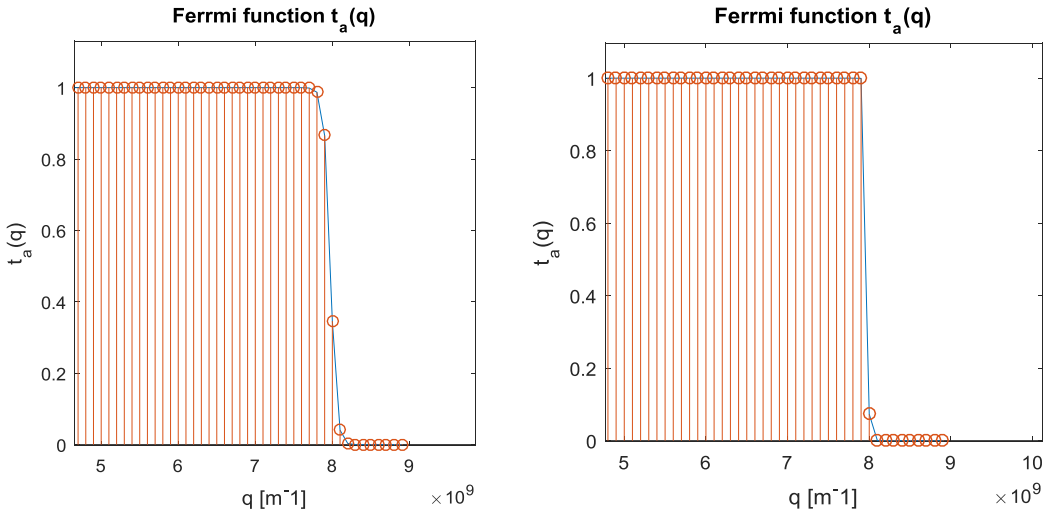

Figure 6.2: Comparison of Fermi function with $\delta a = 0.1$ (left) and $\delta a = 0.05$ (right)

There is the image of the resulting profile of the electron wave in the aperture plane obtained by (2.6).

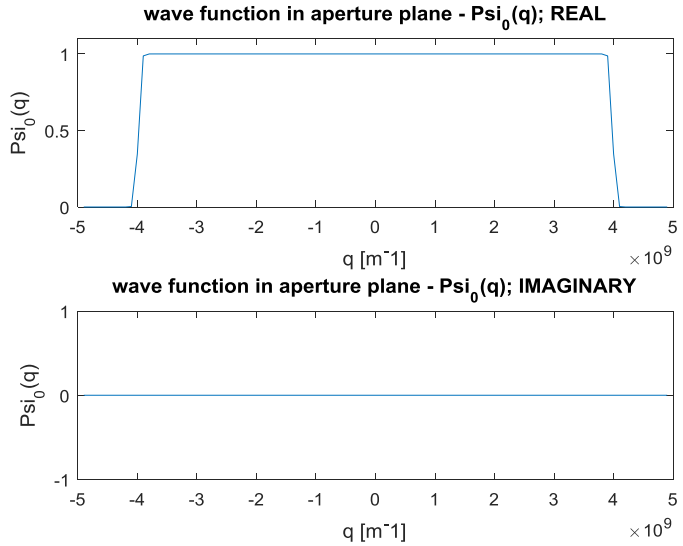

Figure 6.3: Profile of electron wave in the aperture plane (C_1 = 0 nm, C_3 = 0 mm, δa = 0.1, *Uacc* = 200 kV, α = 10 mrad, $q_a = 4 \cdot 10^9$ m^{-1})

As you can see, it is a complex function that corresponds to complex wave function in the aperture plane. Moreover, in this case of present of an ideal objective lens (C_3 = 0 mm), the phase (imaginary) part is constant.

Now, the 2D input matrix of Fourier transform can be obtained. This is performed by rotating of this profile around axis using distance map and interpolation. First, the 1D distance vector of the profile is generated. This vector contains distance values (measured in pixels) from the center of the vector of profile, so that its length is same as length of the vector of the profile. Then, the distance map is generated on the basis of Euclidean distance from the center of distance matrix, using the distance vector as a pattern for x and y axis of the distance matrix. So that, the distance matrix contains values of Euclidean distances from the center of the matrix. Finally, values of the profile vector are interpolated to the distance matrix using the distance vector values, which correspond to the values of the profile vector. So that, the resulting matrix is square with the same side length as the length of the profile vector.

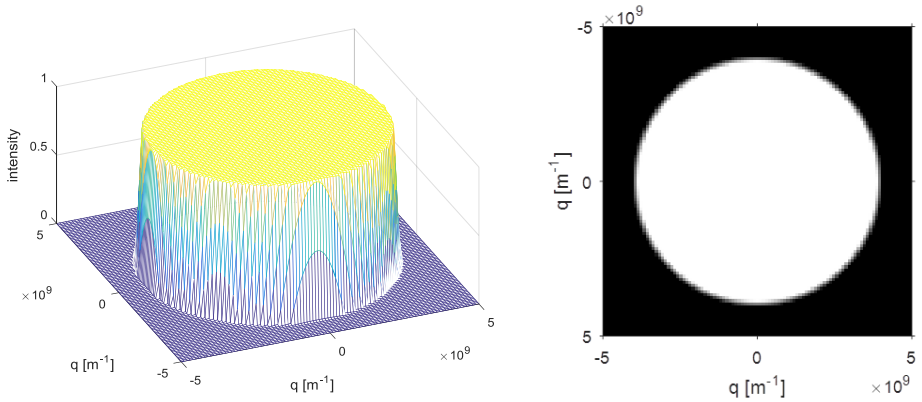

Figure 6.4: Electron wave in the aperture plane (C_1 = 0 nm, C_3 = 0 mm, δa = 0.1, *Uacc* = 200 kV, α = 10 mrad, $q_a = 4 \cdot 10^9$ m^{-1})

Then the computation using Fourier transform can be performed, using 2D Fast Fourier transform algorithm (*fft2* command in MATLAB). As mentioned before, in order to get required sampling frequency, the signal (matrix) has to be completed by nulls to required length (size). So that, in the case of $F_S = 10^{11}$ m^{-1}, the size of the input matrix is 10^3x10^3, that allows quite quick computation. In the case of $F_S = 10^{12}$ m^{-1}, the size of the input matrix is 10^4x10^4, that provides better final precision but at the cost of higher computational demands. This adding of nulls is performed using *fft2* command.

So, after Fourier transform of this signal, we obtain the 2D complex sinc-like signal of the electron wave in the specimen plane. Then, the modulus of this signal is performed, which represents the intensity of the electron wave in the aperture plane. So that, the Airy pattern signal is obtained.

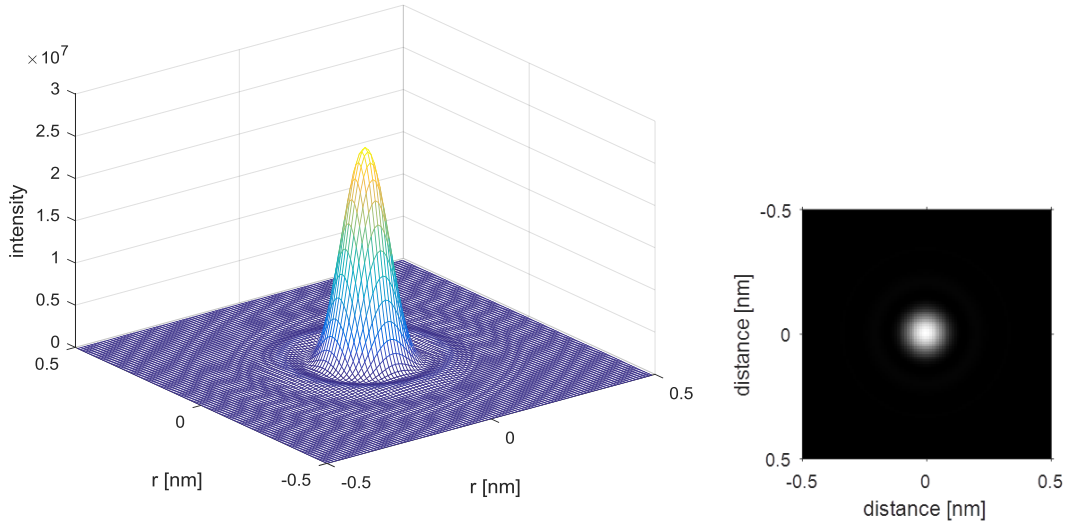

Figure 6.5: Electron wave in the specimen plane (C_1 = 0 nm, C_3 = 0 mm, δa = 0.1, *Uacc* = 200 kV, α = 10 mrad, $q_a = 4 \cdot 10^9$ m^{-1})

At this time, we can extract the profile from obtained Airy pattern to obtain the profile of diffraction-limited electron probe and work with that further.

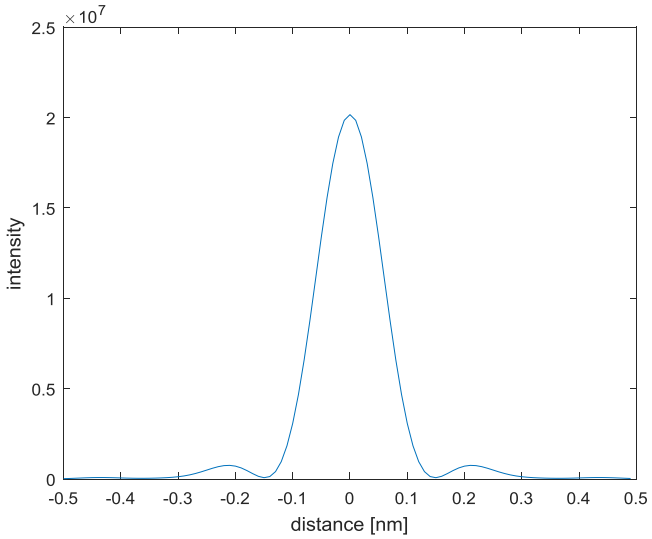

Figure 6.6: Profile of electron wave in the aperture plane (C_1 = 0 nm, C_3 = 0 mm, δa = 0.1, *Uacc* = 200 kV, α = 10 mrad, $q_a = 4 \cdot 10^9$ m^{-1})

As expected, relative to wave optics theory, the width of given main peak is inversely proportional to width of the signal in the aperture plane. This also corresponds to signal theory. Moreover, the proof of the correctness of given result is performed by comparing of widths of obtained Airy patterns to theoretical values obtained by (2.1).

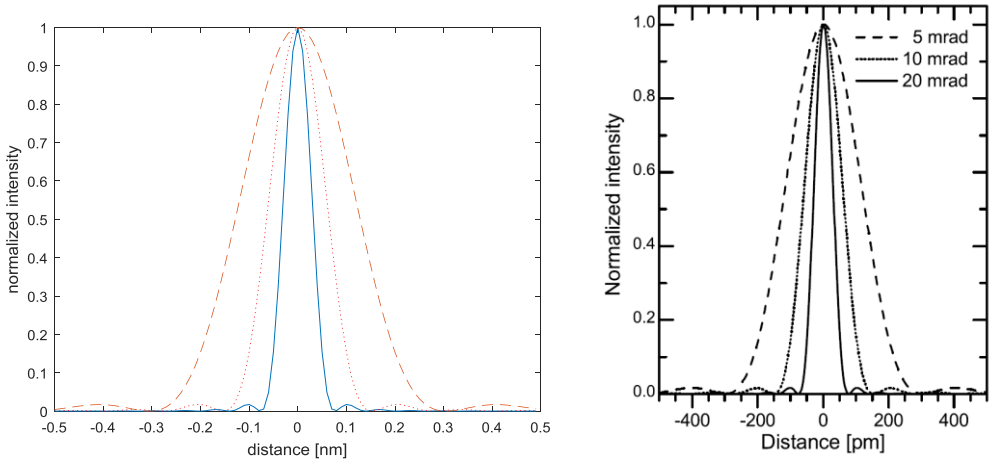

Figure 6.7: Comparison of obtained Airy patterns and these presented in [8] (blue line - 20 mrad, dotted line - 10 mrad, dashed line - 5 mrad)

Nevertheless, it is very interesting that to transition from the frequency domain to the original domain is used forward Fourier transform instead of inverse Fourier transform, as it is common. However, both transformations do essentially the same. The difference between both transformation is only in sign change in the imaginary part of the base function and in the multiplication constant, which staying in front of the transform. The final shape of the result is then essentially the same (Fourier transform of rectangle function is sinc function). The difference is only in the interpretation of the results. In the case of inverse Fourier transform, the result would represent the probability of present of electrons in given place in original domain. On the other hand, the case of forward Fourier transform gives us the result of the result related to the energy distribution, that is more interesting in our case [18].

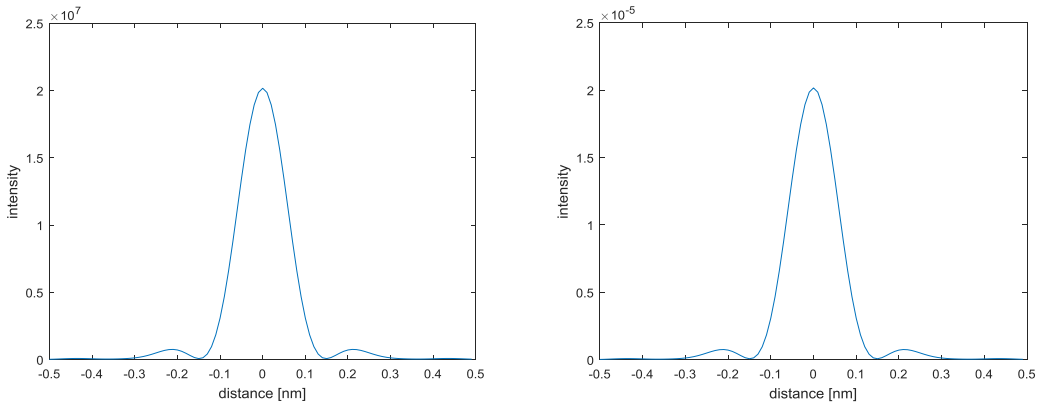

Figure 6.8: Comparison of the result from FT and the result from FT^{-1} (C_1 = -50 nm, C_3 = 1 mm, δa = 0.1, *Uacc* = 200 kV, α = 10 mrad, $q_a = 4 \cdot 10^9$ m^{-1})

6.1.2 Spherical aberration and defocus

Now, the influence of the spherical aberration and defocus is incorporated. They are described in the aperture plane by the aberration function (2.5), which essentially modifies the electron wave function in the aperture plane (2.6). This incorporation is performed very simply – the constant of spherical aberration is just nonzero, than in the previous case. However the constant of defocus C_1 is not limited in both cases: the diffraction case and the spherical aberration case. Nevertheless, for better demonstrating of diffraction, the defocus was set to zero.

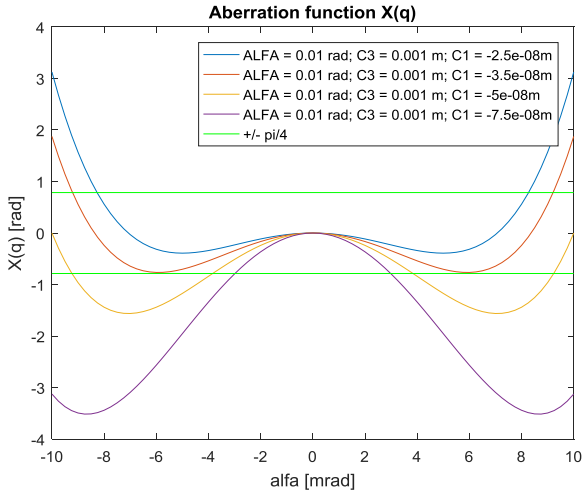

Figure 6.9: Aberration function

So that, the computation is same like in the previous case of diffraction, only the input and output matrix are different. For repetition: the profile of the electron wave in the aperture plane by (2.6) is obtained, but in this case its shape is influenced by nonzero C_3. Than the 2D electron wave is obtained and 2D Fourier transform is performed. The resulting intensity represents the diffraction-limited and spherical-aberration limited electron probe. Finally the profile of the electron probe is extracted like in the previous case. However, in this case, the profile is additionally affected by spherical aberration.

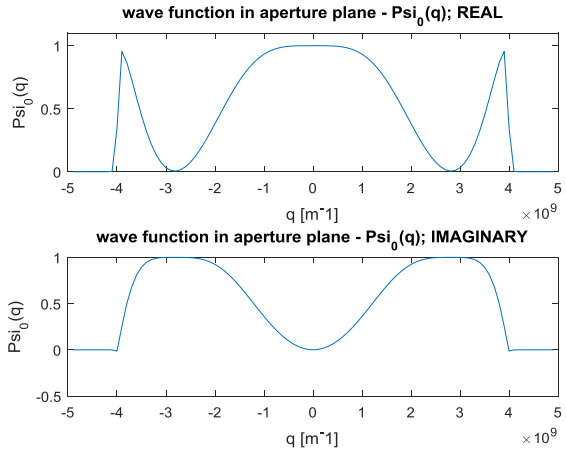

Figure 6.10: Profile of electron wave in the aperture plane (C_1 = -50 nm, C_3 = 1 mm, δa = 0.1, $Uacc$ = 200 kV, α = 10 mrad, $q_a = 4 \cdot 10^9$ m^{-1})

The spherical aberration essentially modifies the phase part of the electron wave function. It also modifies the amplitude part, but the phase shifts in the in the imaginary part are more crucial. It causes the change in the interference on the specimen plane and thus the distortion of Airy pattern. The amplitude part is modified because in order to preserve total energy in the specimen plane, during the distortion.

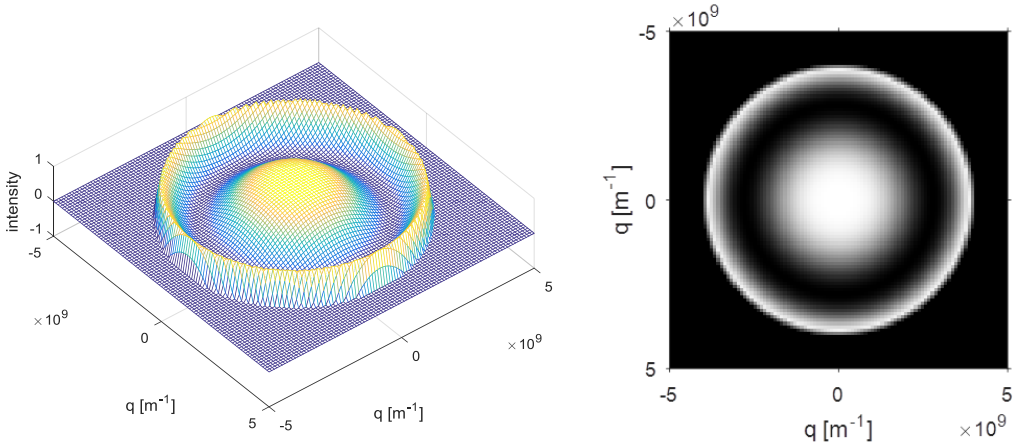

Figure 6.11: Electron wave in the aperture plane (C_1 = -50 nm, C_3 = 1 mm, δa = 0.1, $Uacc$ = 200 kV, α = 10 mrad, $q_a = 4 \cdot 10^9$ m^{-1})

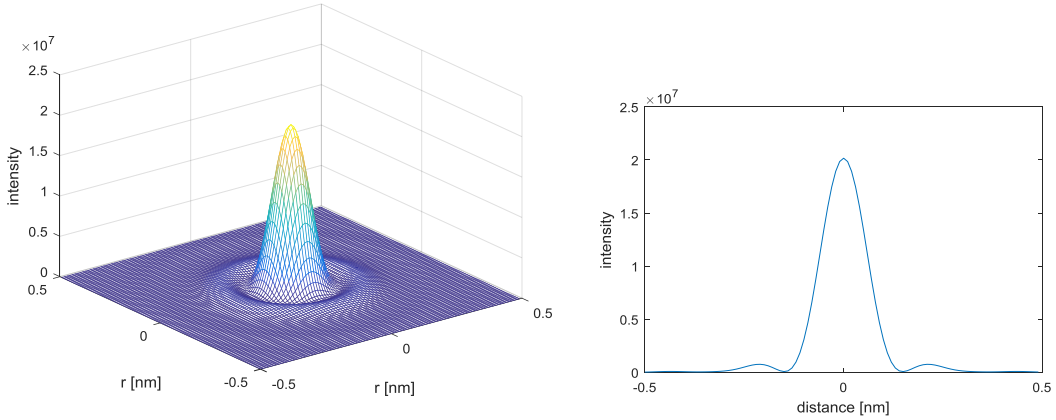

Figure 6.12: Electron wave in the aperture plane(left) and its profile (right) (C_1 = 0 nm, C_3 = 0 mm, δa = 0.1, *Uacc* = 200 kV, α = 10 mrad, $q_a = 4 \cdot 10^9$ m^{-1})

6.1.3 Incorporating of real finite electron source

Both cases of the electron probe profile obtaining described above assume the point-like source. However, real sources have finite size described by the source intensity distribution function *S(r)*. In our case, we approximate this function by Gaussian function, which is sufficiently suitable. The incorporation is given by convolution between this function and the electron probe profile limited by diffraction and/or spherical aberration (2.15).

In this case, the computation can be performed one-dimensionally. The final precision is not influenced and computational demand significantly decreases.

In the case o FEG sources, after demagnification of their size, we can obtain very small Gaussian spot on the specimen plane. This very small Gaussian spot then influences the final shape of the electron probe only lightly. This means that resulting electron probe profile is more similar to Airy profile than to Gaussian profile.

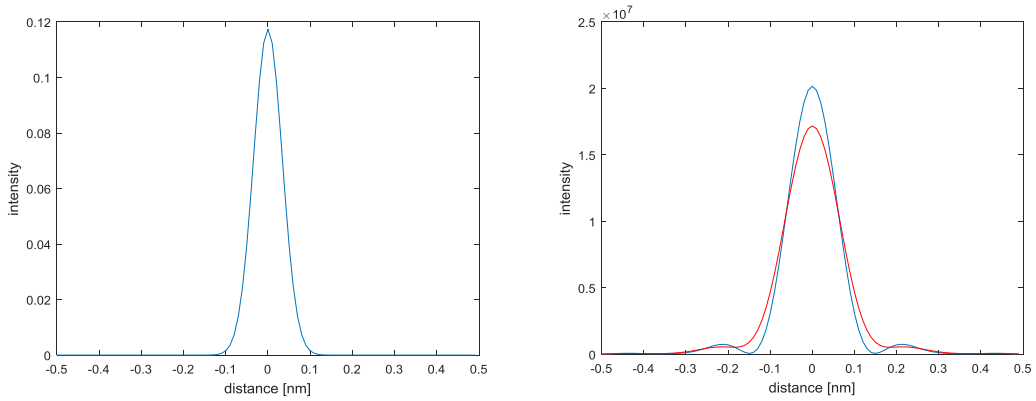

Figure 6.13: Small electron source distribution (left picture); point-like source produced electron probe profile (blue) and electron probe profile of small el. source (red)

On the other hand, in the case of larger sources, their final demagnigied size cannot be so small like in previous case. So that, the Gaussian spot is significantly wider than the profile of diffraction-and-spherical-limited probe. After convolution, the result signal then looks more like Gaussian function

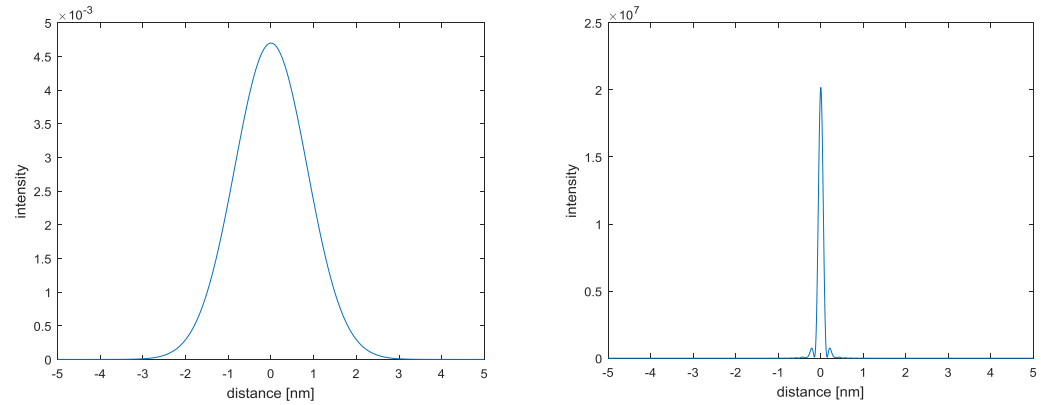

Figure 6.14: Large electron source distribution (left picture); point-like source produced electron probe profile (right picture)

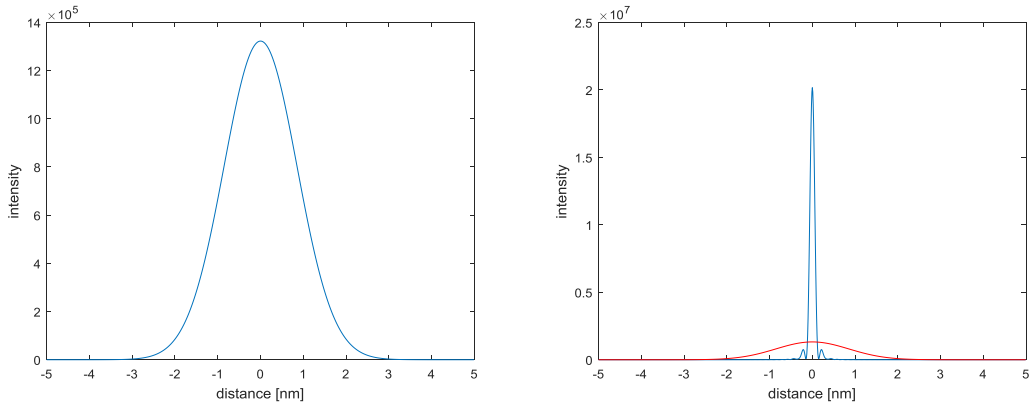

Figure 6.15: electron probe profile of large el. source (left); comparison of electron probe profile of large el. source (red) and point-like source produced electron probe profile (blue)

Moreover, in order to preserve constant total energy, the *S(r)* has to be normalized, in order to its sum is equal to one. This is because the ideal *S(r)* is equal to Dirac impulse whose integral is equal to one, that represents of 100 % of the source intensity in one point. So that, the real *S(r)* has to cover also 100 % intensity of the source.
In the final result, it causes that, the maximum intensity of resulting electron probe decreases. That corresponds to real assumption.

6.1.4 Partial temporal coherence

Final aberration that is incorporated to the calculation is influence of partial temporal coherence and thus influence of chromatic aberration of the objective lens and energy spread of the electron source, described by the Gaussian energy distribution function *T(E)*. So that, this aberration depends on this two parameters, that together influence the value of defocus. The result of that is the spread of defocus around the pre-set nominal defocus (Figure 6.16).

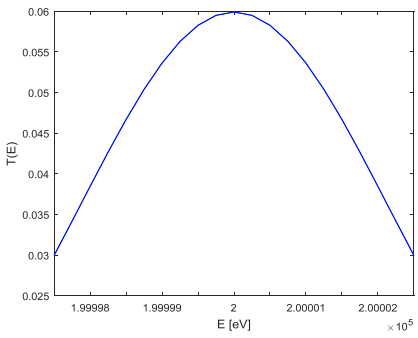

Figure 6.17: Energy distribution function *T(E)*(C_C = 2 mm, δE = 5 eV)

In this case, the computation can be also performed one-dimensionally, which the most significantly reduces computational demand. So that, for every given value of energy (defocus) of the whole energy spread (defocus spread), the electron probe profile is calculated as described above. The final result is then given by sum of these partial results.

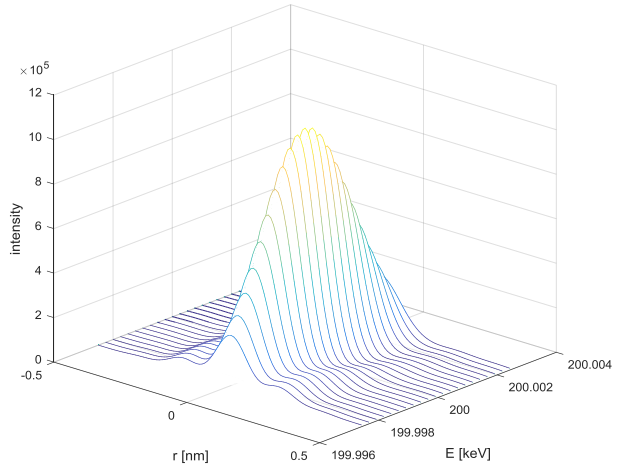

Figure 6.18: Electron probe profiles, calculated for different electron energy of electron energy spread and then weighted by *T(E)*

The *T(E)* then weights the contribution of every computed probe profile (for given *E*). The *T(E)* has to be also normalized, in order to its sum is equal to 1. The reasons are the same like in the case of the real-source-size part - to preserve constant total energy of the source. If the source is monochromatic, the *T(E)*would be equal to Dirac impulse and thus to value 1 (100 % of source intensity on this one single electron energy).

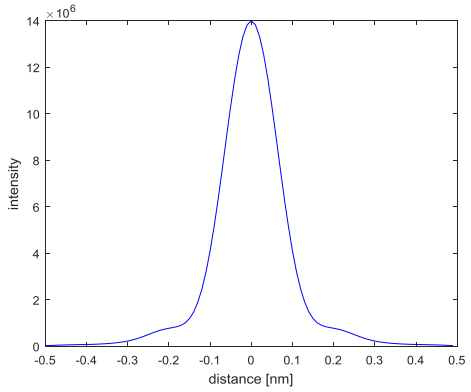

Figure 6.19: Profile of final electron probe, that includes all mentioned aberrations (C_1 = -50 nm, C_3 = 1 mm, C_C = 2 mm, δa = 0.1, *Uacc* = 200 kV, α = 10 mrad)

6.2 Modelling of the PSF

After obtaining the final electron probe intensity profile, the point spread function can be finally created. This is performed by rotating of this profile around axis using distance map and interpolation. This process is more detailed described in the section of diffraction. Final PSF is then square matrix with the same scale and resolution as the electron probe intensity profile.

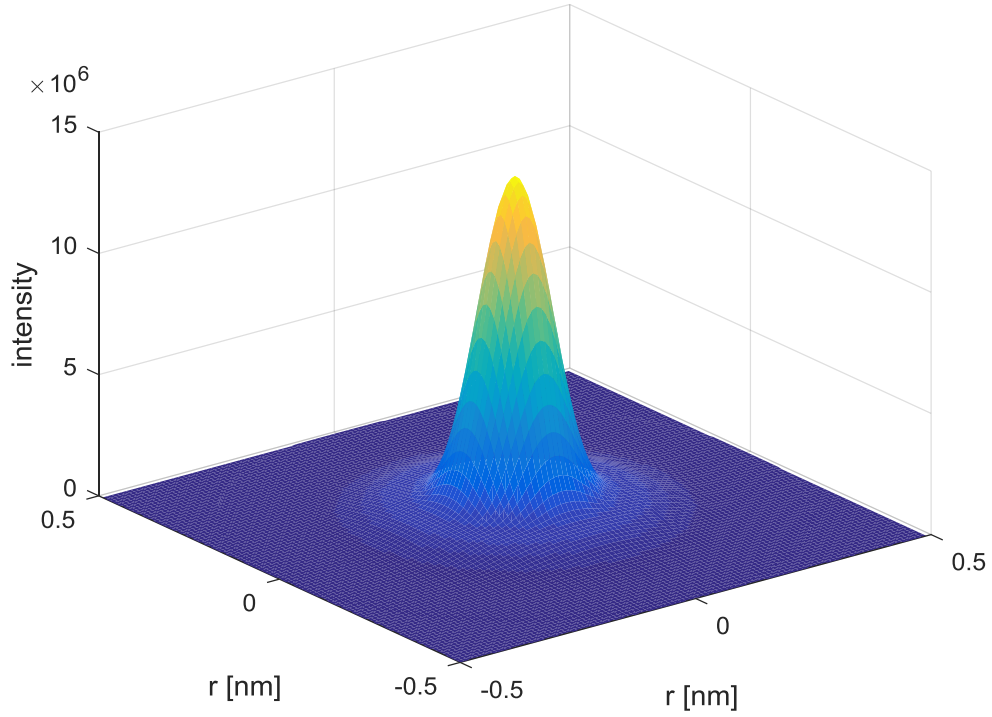

Figure 6.20: Final electron probe

6.3 STEM PSF simulator

Because of that, the simulation of the STEM point spread function works well, it was decided to create a simulation tool, which allows user to model such a PSF as he will desire. User can use this tool to look how given parameters influence shape of resulting PSF or he can use it directly to generate such a PSF, that corresponds to shape of real spot of his device and use it to image deconvolution.

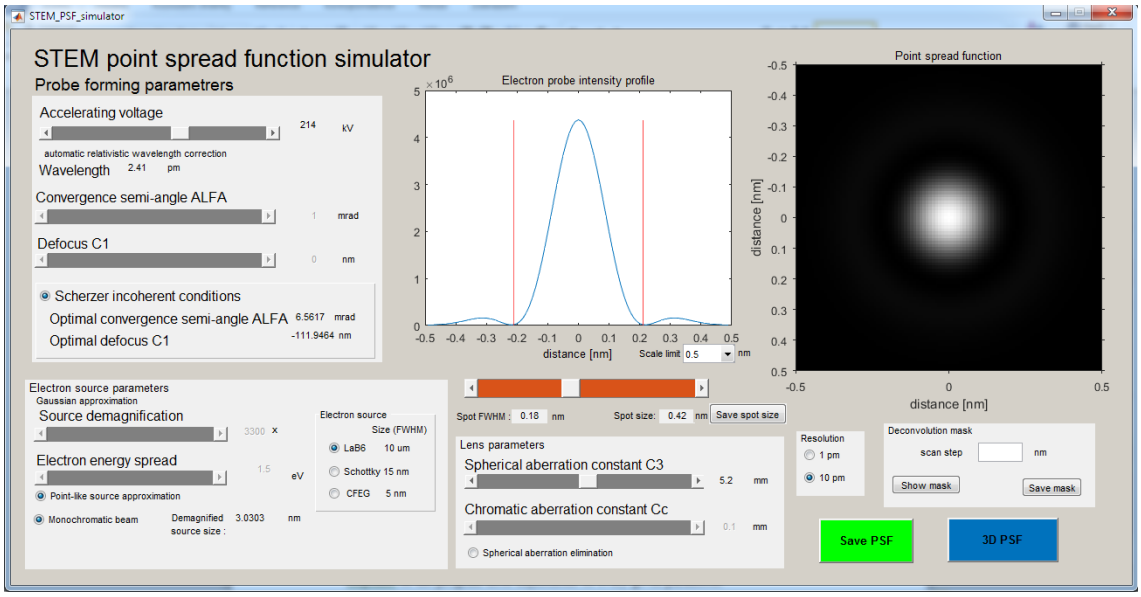

Figure 6.21: STEM point spread function simulator

User can adjust all the parameters by sliders, which allows instantaneous response of the program after adjustment of every given parameter.

So, there are several parameters, that user can adjust by himself. Probably all of them were mentioned before, but for purposes of revision, these are the parameters: acceleration voltage U_{acc} with range from 80 to 300 kV.. Electron wavelength, that corresponds to set U_{acc}. However, the wavelength of accelerated electron have to be relativistic corrected. This is necessary, because already form U_{acc} = 80 kV, the difference between the relativistic corrected value of the accelerated electron wavelength and the value of classical calculation is 4,83 % [33].

The spherical aberration constant C_3 is set in range from 0.1 mm to 10 mm. The minimum value is set for possible simulation of spherical aberration correction. The maximum value is set for higher tool variability

The spherical aberration constant C_C is set with the same parameters and for the same reasons.

Moreover, there is an option to choose setting of Scherzer incroherent conditions, which set the optimal convergence semi-angle α and defocus relative to selected value C_3.

The defocus range and the range of α are set over the optimal Scherzer range. The range of defocus is set from -200 nm to 0 nm and the range of α is set from 1 to 50 mrad. The reason is same as in the case of spherical aberration - higher tool variability. For the same reason, some unreal parameters are set too. There are choice of point-like source, choice of monochromatic beam and choice of spherical aberration elimination. So that, for example when all these unreal parameters are set, the resulting PSF is only diffraction-limited. So that, this allows to show, how could the electron probe looks like theoretically.

There is also incorporated the option of electron source type selection. User can choose from three types of sources: LaB_6, Schottky FEG and CFEG. The wolfram electron source is neglected, because of its insufficient parameters for the case of STEM imaging. All these sources are characteristic with their range of electron energy spread and their source size. The range of electron energy spread changes relative to selected electron source type. However, in order to incorporate the simulation of monochromator use, the minimum value of every electron spread range is set to 0,2 eV. The electron source size is given for every electron source type and its size can be adjusted by parameter of source size demagnification.

The default resolution is set to 10 pm. The program response with this resolution is quite quick, but only in case when the choice of monochromatic beam is set and thus se partial temporal coherence is off. However, this aberration is activated, the program response is little bit slower. There is also possibility to set the resolution to 1 pm. This option allows user to get the more accurate result. However, it is recommended after setting of desired result on the lower resolution, because this option increases computation demand and program response. The response is then several seconds or several tens of seconds (increases with scale range). However, the longest response is when the partial temporal coherence is activated. Then the response is several minutes.

The scale range is set between 0,5 and 5 nm, which is sufficiently suitable for zoom of small electron probes, that are prefer in the case of STEM imaging.

Finally, after adjusting of desired result, user has three options. He can generate the 3D model of his result, he can save his result in the form of raw data or he can generate the deconvolution mask.

First option is very simple. User just click on the blue button “3D PSF” and 3D model is generated and displayed.

Second option is very simple too. User click on the green button “Save PSF” and the all necessary data are saved as a matlab structure (.mat). This structure contains the vector of electron probe profile values, the matrix of PSF values, three matrices of *x,y,z* values for 3D generating, the distance axis corresponding to the electron probe profile vector, information about given resolution and another structure contains all the probe forming parameters and their adequate values.

Third option is simple too, but not as in previous two cases. After adjusting of final result user use the red slider to select desired part of electron probe profile that he want to have in the deconvolution mask. This is very simple and intuitive because when user move with the red slider, in the same time, two red lines appear in the plot and they move according to the red slider. Moreover, this option can also serve as a measure, because below the slider, there is actual spot size value that corresponds to actual width of selected part of electron probe profile.

After this selecting, user has to click on the button “Save spot size”. Then user only has to set the scan step (with decimal comma) value to the edit window on the right side. When he adjusts some probe forming parameter and changes the electron profile shape, he has to select and save the desired part of electron probe profile again. This is because of robustness. User is than always sure, that the selection is correct. Finally, user can display the deconvolution mask or save it as an image.

Deconvolution mask is generated as an image in uint16 format due to higher precision of the mask. Mask is also automatically modificated, so that its size is always odd. This is performed by adjusting the selected part of electron probe profile, because the scan step has to be constant for given case.

7 TESTING

This chapter deals with the testing of created model relative to its use for non-blind deconvolution. However, first, the evaluation methods are tested in order to verify their proper functioning. Then the background noise estimation of real STEM images is performed. Finally, results of Lucy-Richardson deconvolution of real and model images are presented.

7.1 Evaluation methods

In the theoretical part of this work, as the criterion of similarity, the RMSE function, the Image Quality Measure (sharpness measure) and the Histogram Spread (HS) (contrast measure) is decided to use. The RMSE is quite common evaluation methods, but the other two methods are not. So that, it was decided that their proper functioning should be tested before the data testing.

First, the HS is tested. In the beginning, the evaluation data have to be created. This is performed using classical Lena image, whose contrast is adequately adjusted in order to obtain desired data. So, there is contrast testing data set. The first image of the data set is original Lena image. The second image has equalized histogram and contrast of the rest two images is transformed in order to obtain their overexposed and underexposed version.

Figure 7.1: Contrast verification data

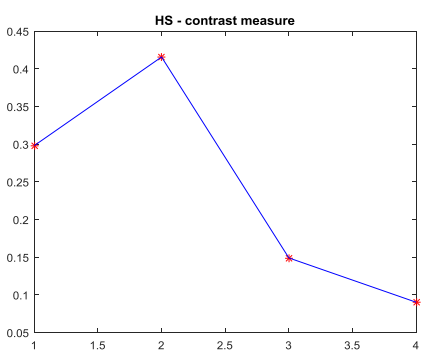

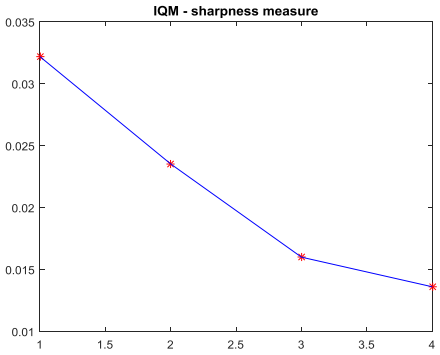

Figure 7.2: Contrast verification Figure 7.3: Sharpness verification

This plot then represents final results of the HS. The points of this plot correspond to the sequence of evaluation images. The results are essentially as expected. The first HS value of the original Lena is quite high however the value that corresponds to the adjusted image is higher as expected. The rest two lower values are correct too since they represent low-contrast images.

The testing of the Image Quality Measure has the same procedure. First, the evaluation data are created, also using the Lena image. However, in this case, this image is gradually blurred. As the blurring kernel, the 9x9 Gaussian filter mask is used. The standard deviation *sigma* of the Gaussian profile is gradually increased from. So, there is sharpness testing data set contained of the original Lena image as the first and then there are blurred images by the filter mas with the *sigma* of 1, 2 and 3.

Figure 7.4: Sharpness verification data

The resulting values are as expected too. The first original Lena image has the best contrast by this measuring technique. The other values then gradually decrease relative to increasing of the *sigma* and thus increasing of image blurring.

7.2 Noise estimation

In the deconvolution, the Lena image is used as model image. However, first, this image has to be blurred by obtained STEM point spread function, which represents the blurring of the STEM device. Nevertheless, in real STEM images, the noise is presented too and in order to get the best possible model image, this noise has to be estimated.

The estimate is as follows: first, some homogenous area of a STEM image without useful signal is separated. This area then represents background noise of STEM images. Then, the histogram of this area is obtained. This histogram is then normalized, in order to its sum is equal to zero. So that, its values corresponding with given shade of grey then represents the probability of given shade. Finally, the *randpdf* function is used, that generates pseudorandom image of given noise. The input variables of this function are the information of grayscale, the information of probabilities corresponding to the grayscale and the dimension of desired output image (size of the Lena image in this case). The resulting matrix than corresponds to given background noise, which is then added to the original Lena image.

Although, the noise level changes with the dwell time, so that this estimation is performed for all dwell time possibilities of our real testing data.

7.3 Results

In this section, evaluation of results of Lucy-Richardson method is performed. The testing is performed on model data and real data. The real data are captured by STEM microscope from Thermo Fisher company. The electron source of this device was LaB_6 and the accelerating voltage was 120 kV. In the picture below you can see the measured profile of electron probe, which was set at that time and by which, the measuring was performed. This measured spot profile then serves as a pattern for generating of simulated PSF that should correspond to that measured PSF (profile).

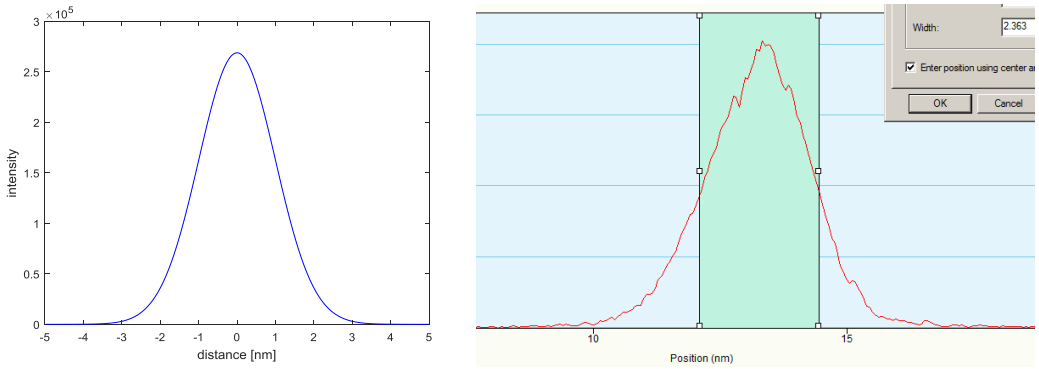

Figure 7.5: Simulated spot profile (left), measured spot profile (right)

For adequate evaluating, the model data have to be adjusted before testing. The Lena image represents the original image (scene) that we do not now in the case of STEM. In the case of STEM, we have just images of blurred and noised scene, that is captured by this device. Hence, the model data have to be blurred with the simulated PSF and then adequately noise.

Both image forming acquisition parameters are tested: dwell time and magnification. They are tested also in both cases – model and real data.

As a deconvolution method is set the Lucy-Richadrson method, that is determined as the best in the theoretical part of this work. This method is implemented in MATLAB by command *lucydeconv*. However, in order to compare this implementation, the deconvolution si performed also by ImageJ program, especially by its DeconvolutionLab2 plugin.

Nevertheless, it was detected, that in deconvolved images, there is presented some edge artefact. So that, before evaluating of given deconvolved images, the edges of these images are cut, in order to avoid inaccuracy in measuring.

7.3.1 Testing on model data

First, the results of deconvolution of model data are presented. These data are presented from minus one iteration, which represents the original unblurred image. Then, the zero iteration represents the initial noised and blurred Lena image that is the input to the Lucy-Richardson deconvolution. The other iterations then correspond to given deconvolution results. So that, in the case of model data, the first value (iteration -1) corresponds to the best resulting value, relative to given evaluating method.

DWELL TIME INFLUENCE

In the case of the RMSE, the trend is quite similar in both cases – matlab and ImageJ. The plot shows that, there are relatively big changes in deconvolved images in the first five iterations. After that, this trend gradually stabilizes. In the case of matlab, values converge to zero instead of the ImageJ.

However, in the case of contrast, the ImageJ gives better results, as can be seen in the plot and in given images. The contrast decreases quite fast in matlab deconvolution.

From point of view of sharpness, the plot shows, that matlab gives better result, but this result could be distorting, because in given images, there is present specle noise, that is not present in the images from ImageJ so much. It is especially in the case of dwell time 15 μs with matlab deconvolutin that amplifies the noise. The ImageJ does not have this problem with the noise.

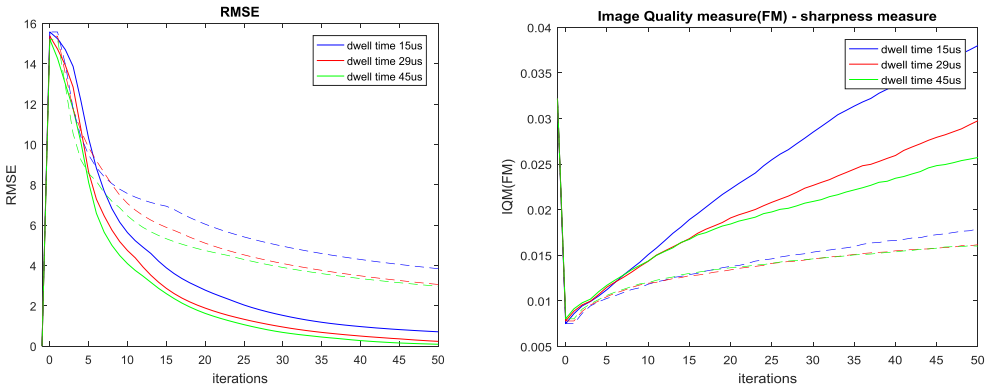

Figure 7.6: Model data dwell time influence (ImageJ – dashed line, MATAB – full line)

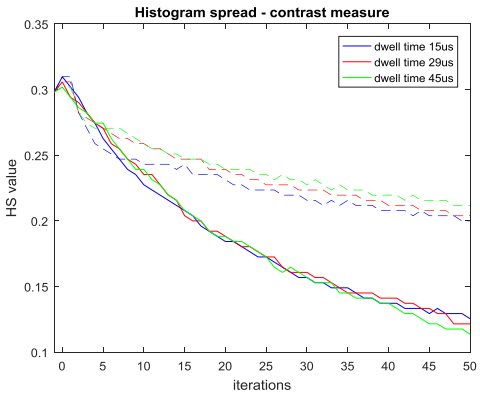

In this picture, there you can see the comparison of matlab deconovolution and ImageJ deknvolution at 50th iteration with 45 μs dwell time. It can be seen, that ImageJ produces better results. In the case of matlab, the contrast decreases with iteration increasing. Moreover, the amplified noise is lightly presented.

Figure 7.7: blurred image (1.), MATLAB result (2.),ImageJ result(3.); 50 iteration, 45μs dwell time, 780k magnification

In the first left picture of this set, there you can see that decovnolution in matlab (20^{th} iteration) converges faster than ImageJ (50^{th} iteration, picture above), but at expense of light noise amplification. Then, there is the comparison of matlab deconovolution and ImageJ deknvolution at 50^{th} iteration with 45 μs dwell time. Again, ImageJ results looks better, due to matlab high noise amplification in this case.

Figure 7.8: MATLAB – 20 iterations, 45μs dwell time (1.), MATLAB – 50 iterations, 15μs dwell time (2.) ,ImageJ – 50 iterations, 15μs dwell time (3.),

So, we can conclude general result, that ImageJ deconvolution produces better results because matlab deconvolution amplifies noise. Although, matlab converges faster, it is at expense of the noise amplification. Moreover, generally, the results show, that the higher dwell time means better result as expected, because it also means higheR SNR.

MAGNIFICATION INFLUENCE

From the point of view of the RMSE, the trend is quite similar – first, fast decrease in the beginning and slow convergence then. The trend in sharpness metric is also same. The result show that matlab deconvolution is better, but it is not true, because of the noise as it was derived in the previous case. The trend in contrast measure is the same case – contrast decreases faster by matlab deconvolution.

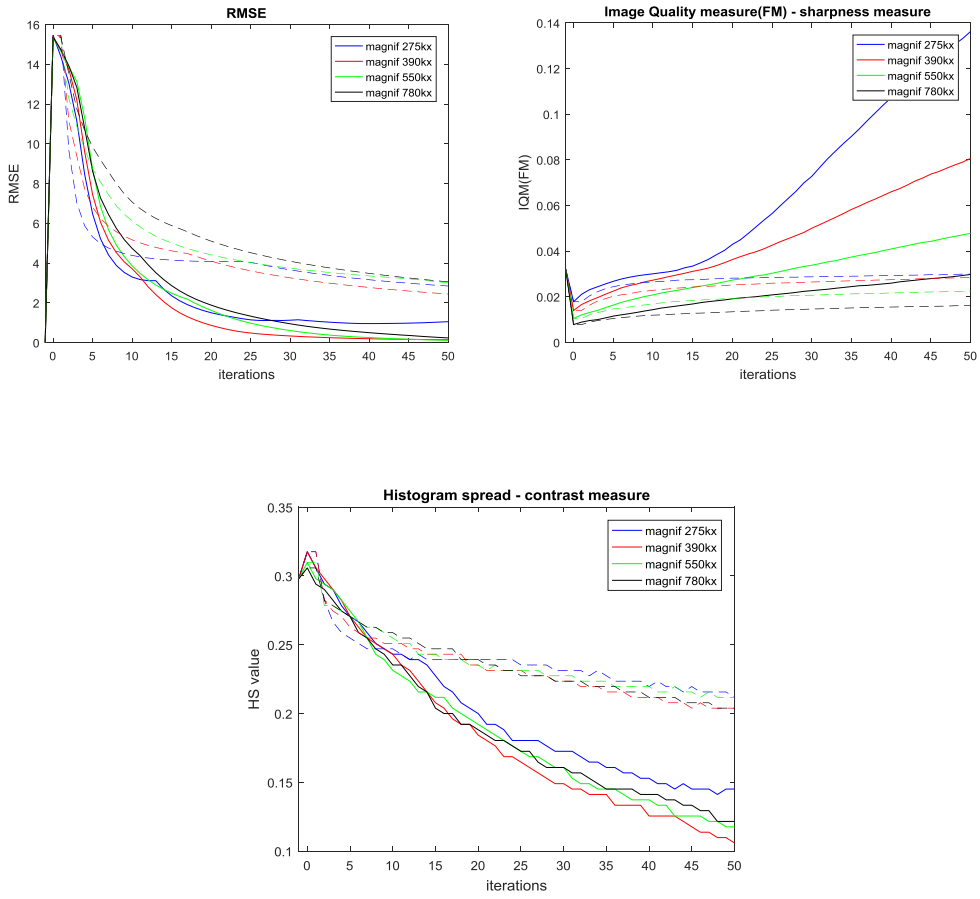

Figure 7.9: Model data magnification influence (ImageJ – dashed line, MATAB – full line)

On these images, there you can see that decovolution results on the model situation are quite good for lower magnifications. Moreover, in the case of matlab deconvolution, there is also seen light noise amplification and contrast decrease.

Figure 7.10: blurred image (left), MATLAB result (middle),ImageJ result(right); 50 iteration, 29μs dwell time, 275k magnification

On these images, there you can see that decovolution results for higher magnifications, which are rather worse. Moreover, in the case of matlab deconvolution, the noise amplification is higher. There is also seen, that matlab deconvolution converges faster, but at expense of noise amplification.

Figure 7.11: blurred image(1.), MATLAB 50 iter.(2.),MATLAB 20 iter.(3.), ImageJ 50 iter(4.); 29μs dwell time, 780k magnification

In the general result, we can conclude, that ImageJ deconvolution produces better results than matlab deconvolution because of noise amplification. Nevertheless, generally, the results on model data show, that the lower magnification means better results. This could correspond to less overlap between electron probes during scanning.

7.3.2 Testing on real data

In the case of real data, the results are presented from zero iteration because there is no original unblurred image. RMSE metric is related to the fist initial original STEM image, that is most blurred. So that, the trend of better results should be inverse, in spite of the case of testing on Lena images. So that, the higher RMSE means better result. The other metrics have same trend like before.

DWELL TIME INFLUENCE

General trend is derived from case of Lena – ImageJ deconvolution procuduces better results than matlab deconvolution – due to fast contrast decrease and noise.

The trend of RMSE shows that, the best results should be in 5^{th} iteration. However, this is not true. The result at 5^{th} iteration is not bad. Its contrast is quite good, but it is still quite blurred too. However, following RMSE values converge to zero, that should mean that, the following results would be worse. In the case of matlab deconvolution, it could be true, but in the case of ImageJ deoconvolution not.

In the case of sharpness measure, there is the same trend like in previous cases. Matlab results looks better, but it is wrong. Moreover, there is the trend, that lower dwell time should be better. This is also not true, as it was derived above.

I the case of contrast, the trend is still the same, the ImageJ gives better results, as can be seen in the plot and in given images. The contrast decreases quite fast in matlab deconvolution.

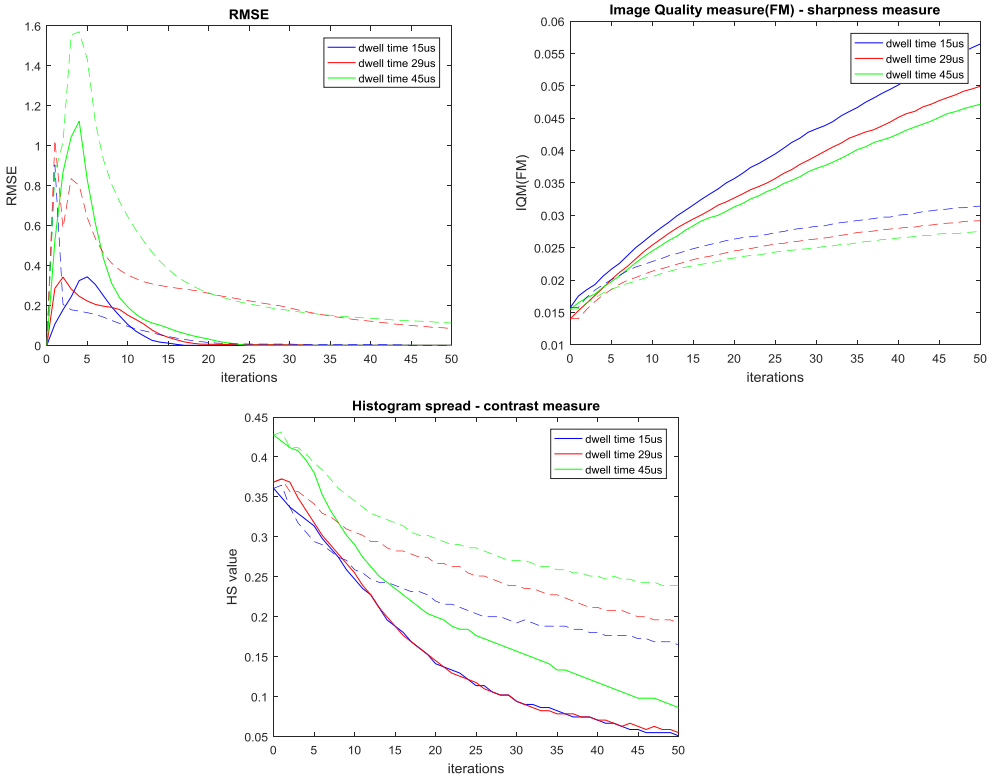

Figure 7.12: Real data dwell time influence (ImageJ – dashed line, MATAB – full line)

In this set of pictures, there you can see the comparison between matlab and ImageJ deconvolution with increasing iteration (from 5th iteration, denoted as the best by the RMSE). There is seen quite quick contrast decrease in the case of matlab.

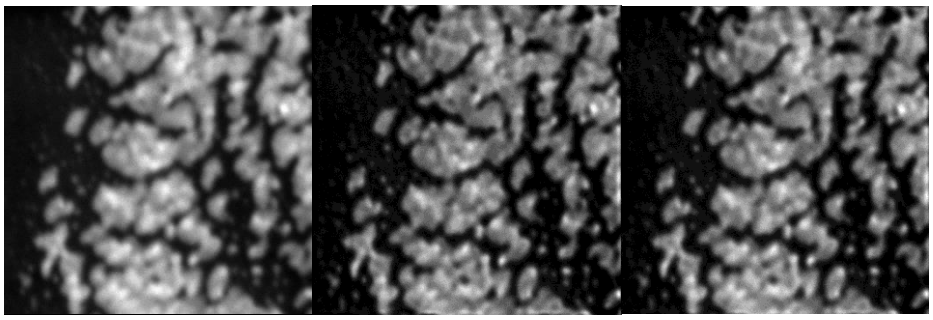

Figure 7.13: original (1), MATLAB result (2.),ImageJ result(3.); 5 iteration, 45μs dwell time, 780k magnification

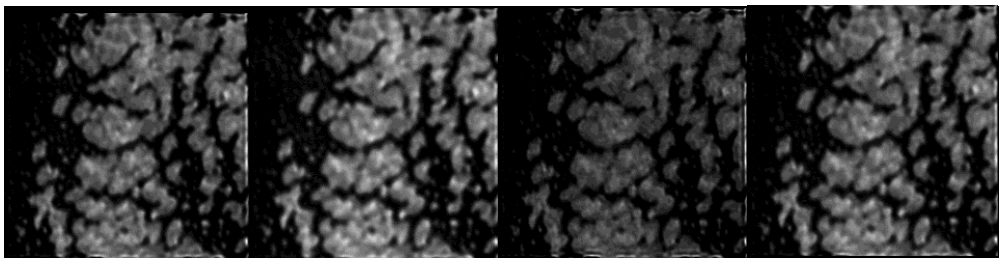

Figure 7.14: MATLAB 10 iter.(1.),ImageJ 10 iter.(2.), MATLAB 20 iter.(1.),ImageJ 20 iter.(2.); 45μs dwell time, 780k magnification

In this set of pictures, it can be seen, that matlab noise amplification is quite big at high iteration (moreover, some circular artefact is present).

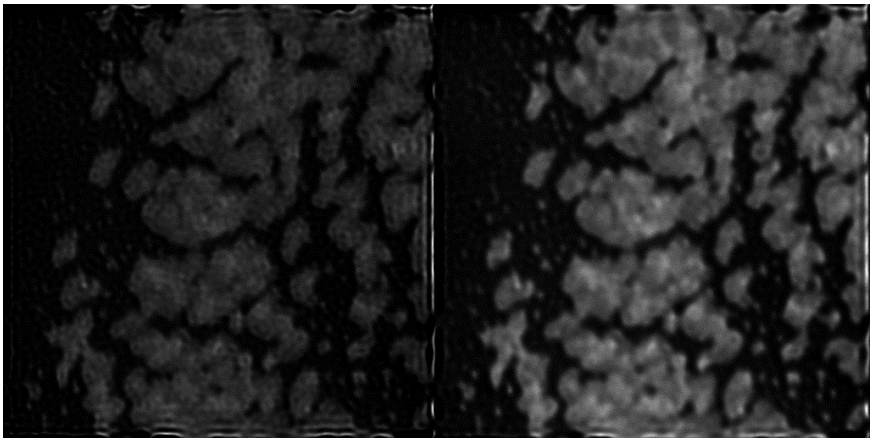

Figure 7.15: MATLAB 40 iter. (1.),ImageJ 50 iter.(2.); 45μs dwell time, 780k magnification

There is the example of relative quick converge of matlab at low iteration, where the noise is not presented yet.

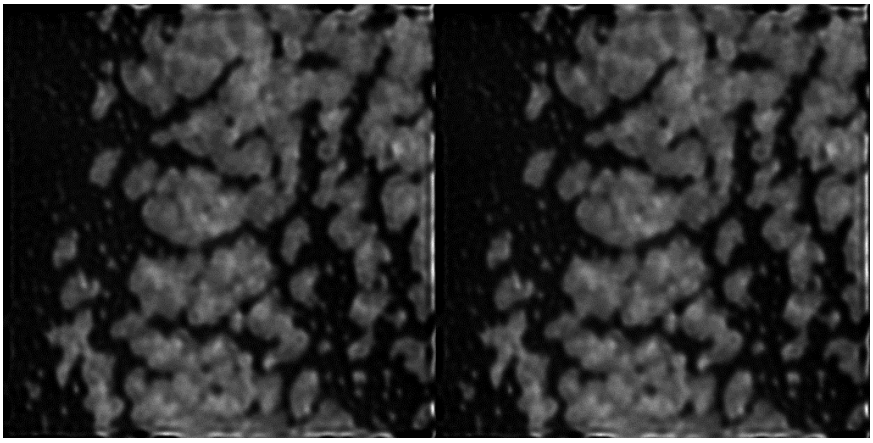

Figure 7.16: MATLAB 15 iter. (1.),ImageJ 50 iter(2.); 45μs dwell time, 780k magnification

In this case, you can see comparison of decovolution resuls for differnt dwell time. The better results should be at higher dwell time, but the contrast of images with dwell time of 29 μs (right) and 45 μs (middle) looks similar. In spite of that, in the image with 15 μs dwell time (left), there can be seen little decrease of contrast.

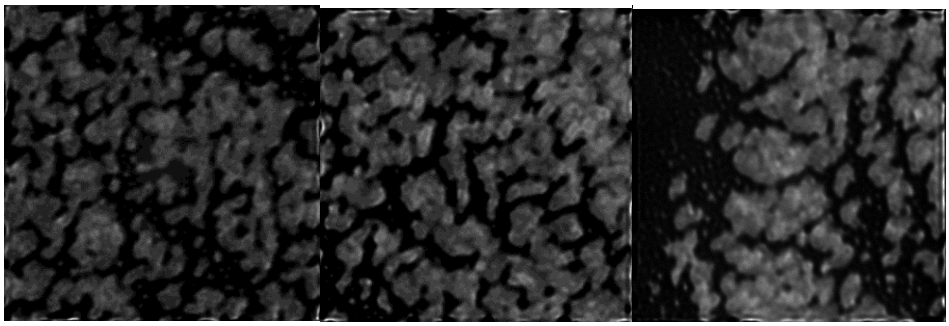

Figure 7.17: ImageJ results - dwell time comparison; 780k magnification, 50 iterations

We can conclude againt, that ImageJ deconvolution produces better results because matlab deconvolution amplifies noise. Although, matlab converges faster, it is at expense of the noise amplification. Moreover, generally, the results show, that the higher dwell time means better result, like in the case of Lena testing.

MAGNIFICATION INFLUENCE

In this case, the RMSE results do not correspond to obtained deconvolved images, so that it should be better to neglect its results.

In the case of sharpness, again, matlab results are showed as the best, but it is wrong. However, the trend, that best results are given for small magnification is there to, like in the case of Lena testing. The reason should be the same – because of small probe overlaps. Moreover, in the case of real data, at small magnifications, images would contain more small object, that can influence this metric.

In the case of contrast, the plot shows that much better results are given for higher magnifications. However, in the of Lena testing, the contrast results are aproximatelly same for all magnifications. Moreover, the lower magnifications have better contrast results in the case of Lena.

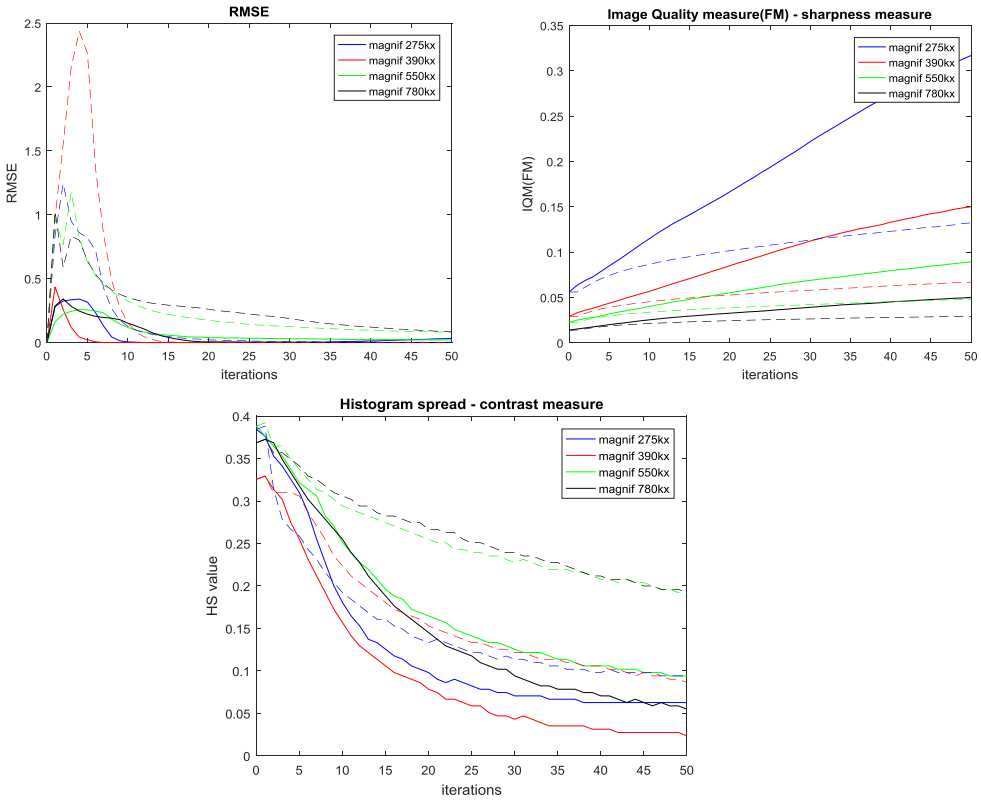

Figure 7.18: Real data magnification influence (ImageJ – dashed line, MATAB – full line)

There is the example of better results for higher magnifications, from the point of view of contrast.

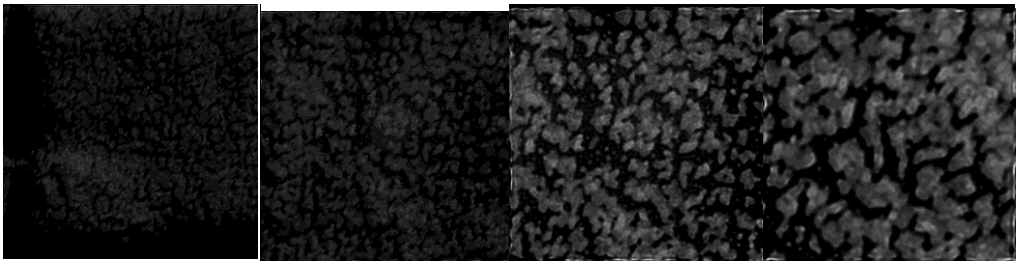

Figure 7.19: magnification: 1. – 275k, 2. – 390k, 3.- 550k, 4 – 780k (ImageJ, 29 μs dwell time, 50 iterations)

In this example you can see comparison between matlab deconvolution and ImageJ deconvolutin, when matlab iteration is low. Then, the result is quite suitable.

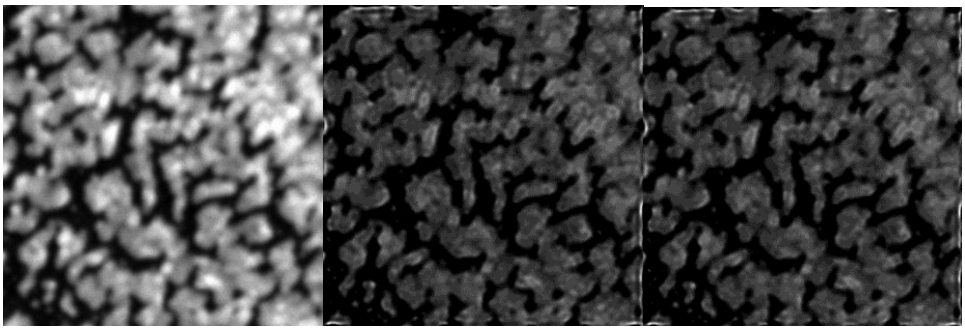

Figure 7.20: Original (1.), MATLAB 15 iter.(2.), ImageJ 50 iter.(3.);(29 μs dwell time, 780k magnification)

In this example, you can see gradual decrease of contrast with iteration increasing, for lower magnification. (29 μs dwell time, 390k magnification)

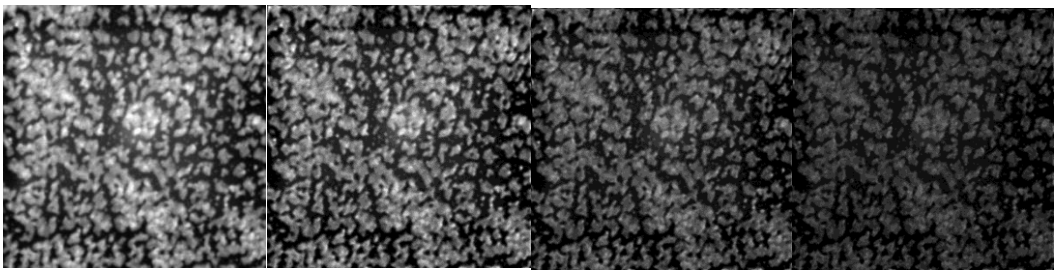

Figure 7.21:Original, ImageJ 5 iter.(1.), ImageJ 10 iter.(2.), ImageJ 20 iter.(3.)

In this example, you can see light decrease of contrast with iteration increasing, for higher magnification. (29 μs dwell time, 550k magnification)

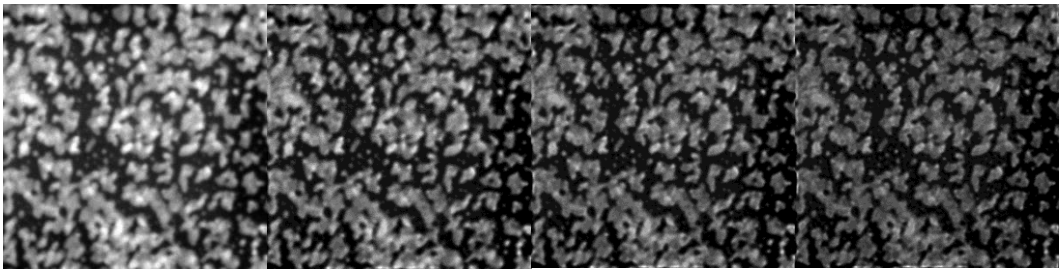

Figure 7.22:Original, ImageJ 5 iter.(1.), ImageJ 10 iter.(2.), ImageJ 20 iter.(3.)

In the general result, we can conclude, that ImageJ deconvolution produces better results than matlab deconvolution because of noise amplification. Nevertheless, generally, the results on real data show, that the higher magnification means better results, because the contrast in low magnified images decrease more significantly. However, the sharpness measure of low magnified images is much higher already at low iterations. This could correspond to less overlap between electron probes during scanning. So that, for them, it is better to deconvolve them maximally to 10^{th} iteration.

8 CONCLUSION

This master thesis deals with the point spread function (PSF) modelling of a Scanning Transmission Electron Microscope (STEM). First, the theoretical research is performed, where the basic description of construction of this device is performed and the key components which have the major influence on the shape of the resultant PSF are determined. Subsequently, the main imaging aberrations that affect the resulting PSF are described. On this base, the PSF model is designed and realized. After that, the resulting PSF model is incorporated to the created simulation tool.

In the realization section, successive steps leading to the resulting model are described. First, the possibility of simplifying of the modelling to 1D is emphasized. This is based on assume of rotational symmetry. However, complications of this simplification and the situation where it cannot be used are described. The realization description starts with the description of the most basic model - the diffraction model. This model forms the basis which is subsequently modified with the incorporation of other aberrations. For this reason, the description of this diffraction model is made most detailed. There are mentioned mainly aspects from the point of view of signal theory, which have to be solved for the success of the whole realization. Subsequently, descriptions of the incorporation of other image aberrations to this basic diffraction model are performed.

Then the resulting simulation tool is descripted. Various parameters that the user can change are described here. These is described their set range, the reason for this setting, and the possible advantages or disadvantages of different settings for given parameter. Then, there are also described instructions for generating a deconvolution mask, which the user has to perform. Subsequently, other options of this tool are described.

Finally, the resulting model is tested. Testing is performed on model data and real data using the Lucy-Richardson method. This method is determined as the best in the theoretical part. Testing with this method was performed in the MATLAB and for comparison, the ImageJ program is used. The results obtained from the testing of model and real data agree each other in some cases, but in some cases it is opposite.

In both cases, the RMSE evaluation method does not seem to be objective. In the case of real data, the resulting RMSE trend does not match with the obtained resulting images. For model data, the trend is correct, but the results show that matlab deconvolution is better. But that's not true. Given method works better in ImageJ. Matlab deconvolution converges faster, but it also amplifies the noise and reduces the

contrast with the number of iterations. On the other hand, ImageJ converges more slowly, but it does not reduce the contrast so fast and does not increase the noise with the increasing number of iterations.

The comparison of the contrast seems to be the most appropriate evaluation method. Here, the trend for both types of data is correct and there is also seen that the ImageJ is better.

The sharpness method also shows relatively good results, but not as good as the contrast comparison method. The trend of this method is correct, but its results show the advantage of matlab deconvolution, which is wrong. This is due to the higher noise amplification in the case of matlab deconvolution that can affect the results.

Anyway, from the point of view of results relative to the acquisition parameters, it has been shown that with the increasing dwell time the quality of the resulting deconvolution is growing, which is mainly reflected in the preservation of the contrast.

In the case of magnification, again from the point of view of contrast measure, better results are detected at higher magnifications. In the case sharpness measure, it is the reverse, but the resulting sharpness in images is degraded by reducing the contrast with number of iterations. So that, the low-magnified images should be therefore deconvolved maximally to 10 iterations. Due to the better results of ImageJ, the results on real data are evaluated using it.

Finally, the possible success of this postprocessing approach can be considered, as well as the possible success of the PSF modelling that is crucial to this approach. The results show that there is some improvement in the images and the information contained in them is emphasized.

In proposing another possible approach one could consider adding real characteristics of electron sources that could improve subsequent deconvolution. In the case of deconvolution, it would be possible to achieve better results by including other input parameters of Lucy-Richardson deconvolution.

BIBLIOGRAPHY

[1] KARLÍK, Miroslav. *Úvod do transmisní elektronové mikroskopie*. Praha: České vysoké učení technické v Praze, 2011.

[2] EDITED BY STEPHEN J. PENNYCOOK a PETER D. NELLIST. *Scanning transmission electron microscopy imaging and analysis*. New York: Springer, 2011. ISBN 978-144-1972-002.

[3] WIGGINS, J. W., J. A. ZUBIN a M. BEER. *High-resolution scanning transmission electron microscope at Johns Hopkins: Imaging and Analysis*. Department of Biophysics. The Johns Hopkins University. Baltimore. Maryland 21218, 1978.

[4] *Learn to use TEM: Astigmatism* [online]. [cit. 2018-01-02]. Available fom: http://www.rodenburg.org/guide/t600.html

[5] *High Angle Annular Dark Field (HAADF) STEM Tomography* [online]. [cit. 2018-01-02]. Available from: http://www-rem.msm.cam.ac.uk/research/CETP/STEM_Tomo.html

[6] *Electron microscopy: STEM Detectors* [online]. [cit. 2018-01-02]. Available from: http://www.microscopy.ethz.ch/STEM.htm

[7] KUBÍNEK, Roman, Klára ŠAFÁŘOVÁ a Milan VŮJTEK. *Elektronová mikroskopie*. Katedra experimentální fyziky a Centrum výzkumu nanomateriálů, Univerzita Palackého v Olomouci, 2011.

[8] ERNI, Rolf. Aberration-corrected imaging in transmission electron microscopy: Chapter 3 Scanning Transmission Electron Microscopy. Hackensack, NJ: Distributed by World Scientific Pub. Co., c2010. ISBN 978-1-84816-536-6.

[9] *Encyklopedie fyziky: Rozlišovací schopnost optických přístrojů* [online]. [cit. 2018-01-03]. Available from: http://fyzika.jreichl.com/main.article/print/525-rozlisovaci-schopnost-optickych-pristroju

[10] ERNI, Rolf. Aberration-corrected imaging in transmission electron microscopy: Chapter 2 High-Resolution Transmission Electron Microscopy. Hackensack, NJ: Distributed by World Scientific Pub. Co., c2010. ISBN 978-1-84816-536-6.

[11] *Fourier Theory* [online]. [cit. 2018-01-03]. Available from: https://users.cs.cf.ac.uk/Dave.Marshall/Vision_lecture/node17.html

[12] *Rectangle function Fourier transform* [online]. [cit. 2018-01-03]. Available from: http://farside.ph.utexas.edu/teaching/315/Waves/img2059.png

[13] *Spherical aberration* [online]. [cit. 2018-01-03]. Available from:

https://photographylife.com/what-is-spherical-aberration

[14] *Chromatic aberration* [online]. [cit. 2018-01-03]. Available from: https://photographylife.com/what-is-chromatic-aberration

[15] *Astigmatism* [online]. [cit. 2018-01-03]. Available from: http://scanning-electron-microscopy.blogspot.cz/2012/07/sem-astigmatism.html

[16] JONES, Lewys a Peter D. NELLIST. Identifying and Correcting Scan Noise and Drift in the Scanning Transmission Electron Microscope. *Microscopy and Microanalysis*. 2013, **19**(04), 1050-1060. DOI: 10.1017/S1431927613001402. ISSN 1431-9276.

[17] SANG, Xiahan, Andrew R. LUPINI, Jilai DING, Sergei V. KALININ, Stephen JESSE a Raymond R. UNOCIC. Precision controlled atomic resolution scanning transmission electron microscopy using spiral scan pathways. *Scientific Reports*. 2017, **7**(04), 43585-. DOI: 10.1038/srep43585. ISSN 2045-2322.

[18] JAN, Jiří. *Číslicová filtrace, analýza a restaurace signálů*. Akademické nakladatelství, VUTIUM, 2002.

[19] OREL, J.: Dekonvoluce biomedicínských obrazů v digitální mikroskopii. Diplomová práce, Masarykova univerzita, Fakulta informatiky, Brno 2006.

[20] *Scientific Volume Imaging: Point Spread Function* [online]. [cit. 2018-01-03]. Available from: https://svi.nl/PointSpreadFunction

[21] SARDER, P. a A. NEHORAI. Deconvolution methods for 3-D fluorescence microscopy images. *IEEE Signal Processing Magazine*. 2006, **23**(3), 32-45. DOI: 10.1109/MSP.2006.1628876. ISSN 1053-5888.

[22] KEMPEN, G. M. P. Van, L. J. Van VLIET, P. J. VERVEER a H. T. M. Van Der VOORT. *A quantitative comparison of image restoration methods for confocal microscopy*. 1997.

[23] *Statistics How To: RMSE: Root Mean Square Error* [online]. [cit. 2018-01-03Available from: http://www.statisticshowto.com/rmse/

[24] DE, Kanjar a V. MASILAMANI. Image Sharpness Measure for Blurred Images in Frequency Domain. *Procedia Engineering*. 2013, **64**, 149-158. DOI: 10.1016/j.proeng.2013.09.086. ISSN 18777058.

[25] TRIPATHI, Abhishek Kumar, Sudipta MUKHOPADHYAY a Ashis Kumar DHARA. Performance metrics for image contrast. *2011 International Conference on Image Information Processing*. IEEE, 2011, 2011, , 1-4. DOI: 10.1109/ICIIP.2011.6108900. ISBN 978-1-61284-861-7

[26] *Electron Microscopy for Dummies* [online]. [cit. 2018-01-03]. Available from: http://www.snaggledworks.com/em_for_dummies/contact.html

[27] TEM and STEM scheme. *EAG Laboratories* [online]. [cit. 2018-01-03]. Available from: http://www.nanoscience.co.jp/knowledge/TEM/knowledge01.html

[28] Wolfram fiber and LaB6 electron source. *Biological Electron Microscopy* [online]. [cit. 2018-01-03]. Available from: http://www.biologicalelectronmicroscopy.com/introduction-to-biological-electron-microscopy.html

[29] Configuration of thermionic electron gun electron gun. *Northern Arizona University: Electron microanalysis core facility* [online]. [cit. 2018-01-03]. Available from: https://nau.edu/cefns/labs/electron-microprobe/glg-510-class-notes/instrumentation/

[30] *Coma* [online]. [cit. 2018-01-03]. Available from: http://hyperphysics.phy-astr.gsu.edu/hbase/geoopt/coma.html

[31] *AP TECH: Etched Tip Cathode Information* [online]. [cit. 2018-05-17]. Available from: http://www.a-p-tech.com/etched-tip-cathodes.html

[32] Rayleigh limit. *Skulls in the Stars: SEM- Schematic Overview. Electron Detection Tungsten Filament Electron Source*[online]. [cit. 2018-01-03]. Available from: https://skullsinthestars.com/2012/06/13/how-well-can-the-government-spy-on-us-via-satellite/

[33] *Electron Motion in Electric and Magnetic Fields: de Broglie wavelength of fast electrons* [online]. [cit. 2018-05-10]. Available from: https://www.didaktik.physik.uni-muenchen.de/elektronenbahnen/en/elektronenbeugung/wellenlaenge/de-broglie-relativistisch.php

LIST OF SYMBOLS, PHYSICAL CONSTANTS AND ABBREVIATIONS

ΔE	electrons energy spread
ΔI	fluctuation of exciting current of the objective lens
ΔV	fluctuation of accelerating voltage
ADF	annular dark-field
A_S	area of electron source
B	brightness
BF	bright field
C_1	defocus
C_3	constant of spherical aberration
C_c	constant of chromatic aberration
CFEG	Cold field emission gun
d_z	diameter of electron source
E_0	nominal electron energy
FEG	Field emission electron guns
HAADF	high angle annular dark-field
HS	Histogram Spread
I	current of electron beam
$I_0(r)$	intensity of the electron probe on the specimen plane
ICTM	Iterative Constrained Tikhonov-Miller algorithm
I_{probe}	electron probe current
LLS	Linear least square method
M	(de-)magnification
MAP	Maximum a posteriori method
ML	Maximum likelihood method

MSE	Mean squared error
NLS	Non-linear least square method
PSF	Point spread function
q_a	radius of aperture opening
r_{geo}	circular area of source radius
RMSE	Root-mean-square error
RTG	X-ray
S	electron source size
S(r)	electron source intensity distribution function
SNR	Signal-to-noise ratio
STEM	Scanning transmission electron microscope
$T(C_1)$	defocus distribution
T(E)	energy distribution of electron source
TEM	Transmission electron microscope
Z	atomic number
α	illumination (convergence) semi-angle
δ_a	fraction of aperture radius.
δC_1	variation of defocus
δ_D	radius of diffraction-limited probe
δ_E	initial dispersion
δE	variation of electron energy
δ_S	radius of chromatic-aberration-limited probe
δ_S	radius of spherical-aberration-limited probe
λ	electron wavelength
π	Ludolf´s number
$\psi(q)$	electron wave in the aperture plane
$\psi(r)$	electron wave in the specimen plane
$\chi(q)$	aberration function